Global and Planetary Change 265 (2026) 105588

Contents lists available at ScienceDirect

Global and Planetary Change

journal homepage: www.elsevier.com/locate/gloplacha

Research Article

An expanded polar record of the Toarcian hyperthermal from Vilyui River Basin (Siberia)

Alicia Fantasia[a,b,*], Thomas Letulle[a,c], Mikhail A. Rogov[d], Alexey P. Ippolitov[d,e], Oleg A. Lutikov[d], Nikolay Zverkov[d], Arnauld Vinçon-Laugier[a], Thierry Adatte[f], Jorge E. Spangenberg[g], Guillaume Paris[h], Jeremy E. Martin[a], Christophe Lécuyer[a], Barbora Krizova[a], Mathieu Daëron[i], Guillaume Suan[a]

[a] Université Lyon 1, ENS de Lyon, Université Jean Monnet, CNRS, LGL TPE, UMR, Villeurbanne 5276, France
[b] University of Fribourg, Department of Geosciences, Fribourg CH-1700, Switzerland
[c] Department of Geosciences, University of Padua, Padua, Italy
[d] Geological Institute of Russian Academy of Sciences, Moscow 119017, Russia
[e] School of Geography, Environment and Earth Sciences, Victoria University of Wellington Te Herenga Waka, Wellington 6012, New Zealand
[f] Institute of Earth Sciences (ISTE), Faculty of Geosciences and Environment, University of Lausanne, Lausanne CH-1015, Switzerland
[g] Institute of Earth Surface Dynamics (IDYST), Faculty of Geosciences and Environment, University of Lausanne, Lausanne CH-1015, Switzerland
[h] Centre de Recherches Pétrographiques et Géochimiques, Université de Lorraine, CNRS, Nancy F-54000, France
[i] Laboratoire des Sciences du Climat et de l'Environnement (LSCE/IPSL), CEA-CNRS-UVSQ, Université Paris-Saclay, Gif-sur-Yvette Cedex F-91191, France

ARTICLE INFO

Keywords:
Hyperthermal
Pliensbachian-Toarcian
Arctic
Geochemistry
Stable isotopes

ABSTRACT

The early Toarcian was characterized by a massive release of carbon and a major hyperthermal event, marking the acme of a series of rapid and profound environmental perturbations that punctuated the late Pliensbachian–Toarcian period (185–175 Ma). It has been suggested that some of these environmental perturbations were accompanied by the waxing and waning of cryosphere reservoirs (ice caps and permafrost) in high-latitude regions. These Early Jurassic environmental perturbations, however, have been reported almost exclusively in open-marine sediments deposited at mid to low paleolatitudes, so that their global impact and underlying causes remain uncertain. Here we report new litho-, bio-, and chemo-stratigraphic data from key Pliensbachian–Toarcian siliciclastic successions in the Vilyui River Basin, which were deposited in a proximal position along the Anabar Shield near the Early Jurassic North Pole. The new stable carbon, sulfur, and radiogenic strontium isotope data combined with robust biostratigraphy allow to identify the Toarcian hyperthermal event confidently. A major increase in sedimentation rates and a shift from cold, nearshore conditions (with high glendonite and sand contents) to a warmer and deeper setting occurred during that time. Rock-Eval pyrolysis data reveal a thermally immature kerogen dominated by terrestrial material, with a higher contribution and/or better preservation of marine organic matter at the very beginning of the Toarcian hyperthermal event, probably due to a decrease in marine oxygenation. Our results broadly support scenarios involving extreme changes in high-latitude environmental conditions across the Toarcian hyperthermal and set the stage for future evaluations of climate changes in polar seas during this key interval of Earth's history.

1. Introduction

The Early Jurassic witnessed a series of rapid climate oscillations and carbon cycle perturbations. The most intense of these events occurred ~182.8 Ma ago during the early Toarcian, when subtropical seas warmed by >5 °C (Suan et al., 2010; Ruebsam et al., 2020a; Ullmann et al., 2020) in less than few hundred millennia (Kemp et al., 2024). Many studies have focused on the Toarcian hyperthermal event, providing evidence that atmospheric CO_2 concentrations increased by >500 ppm (McElwain et al., 2005; Nordt et al., 2022; Ruebsam et al., 2020b), epicontinental seas became more acidic (Müller et al., 2020; Kasemann et al., 2025), sea-level rose globally by >50 m (Ruebsam and

* Corresponding author at: Université Lyon 1, ENS de Lyon, Université Jean Monnet, CNRS, LGL TPE, UMR, Villeurbanne 5276, France
E-mail address: alicia.fantasia@unifr.ch (A. Fantasia).

https://doi.org/10.1016/j.gloplacha.2026.105588
Received 19 January 2026; Received in revised form 22 June 2026; Accepted 24 June 2026
Available online 2 July 2026
0921-8181/

Schwark, 2021; Nordt et al., 2022), continental weathering rates increased two to six fold (Cohen et al., 2004; Brazier et al., 2015; Percival et al., 2016; Kemp et al., 2020). This led to enhanced input of nutrients to the oceans, raising of organic primary productivity (Fantasia et al., 2019), and the dramatic expansion of anoxic and sulfidic waters (Gill et al., 2011; Them et al., 2018; Kemp et al., 2022; Ruebsam et al., 2022). These profound environmental perturbations resulted in a 2nd order mass extinction (Little and Benton, 1995; Caswell et al., 2009; Nikitenko et al., 2013a; Danise et al., 2015; Bucur and Reolid, 2024), a collapse of marine carbonate factories (Trecalli et al., 2012; Krencker et al., 2020), profound changes in marine and terrestrial primary producers (Mattioli et al., 2008; Mailliot et al., 2009; Slater et al., 2019; Ruebsam et al., 2022), and a large-scale turnover of marine and terrestrial vertebrates (Maxwell and Vincent, 2016; Martin et al., 2021; Reolid et al., 2022, 2024). This warming marked the onset of a period of elevated organic burial lasting several hundred thousand years (Boulila and Hinnov, 2017) initially referred to as the Toarcian Oceanic Anoxic Event (T-OAE) (Jenkyns, 1988). It is thought that this event was triggered by intense volcanic activity in the Karoo-Ferrar Province and associated massive release of greenhouse gases into the atmosphere-ocean system (e.g., Courtillot, 1994; Duncan et al., 1997; Palfy and Smith, 2000; Svensen et al., 2007; Suan et al., 2008). Crucially, the strata documenting the highest marine temperatures record a pronounced, 3–4‰ negative carbon isotope excursion (n-CIE) that qualifies the warming episode as a hyperthermal, i.e., a geologically short-lived interval combining evidence for rapid warming and the massive injection of ^{13}C-depleted carbon into the ocean-atmosphere system.

The Toarcian hyperthermal was preceded and followed by other episodes of intense climatic, environmental, and biotic disturbance. These include the 4 °C cooling episode and marine regression marking the late Pliensbachian, the 2–4 °C warming and 2nd order mass extinction defining the Pliensbachian-Toarcian boundary, and the gradual cooling following the Toarcian climatic optimum during the early–late Toarcian transition (Krencker et al., 2014; Korte et al., 2015; Ferreira et al., 2019; Ruebsam and Schwark, 2021). Several studies (Suan et al., 2010; Ruebsam et al., 2019; Ruebsam and Schwark, 2021) have suggested that some of these various Early Jurassic environmental perturbations were accompanied by the waxing and waning of cryosphere reservoirs (ice caps and permafrost) in high-latitude regions, with emissions of ^{13}C-depleted carbon from permafrost possibly acting as key amplifiers of carbon cycle anomalies. These events, however, have been almost exclusively reported in sedimentary archives from mid to low paleo-latitudes, so that their global nature and underlying causes remain highly uncertain in the absence of well-documented high paleo-latitude records.

Lower Jurassic marine strata deposited at polar paleo-latitudes are widely distributed in northern Alaska, northern Canada, Siberia and northeastern Russia and have been well documented in terms of micro- and macro-fossil assemblages (Devyatov et al., 2010; Nikitenko, 2008; Rogov et al., 2023b). However, these records have been rarely analyzed for stable isotope composition, meaning that the Early Jurassic climatic upheavals remain loosely constrained stratigraphically. One notable exception concerns the T-OAE n-CIE, which has been documented in biostratigraphically well-dated, organic-rich strata from the Polovinnaya River and Kelimyar River region in NE Siberia (Suan et al., 2011; Nikitenko et al., 2013b; van de Schootbrugge et al., 2020). The best-dated and most continuous successions of the Kelimyar River, however, were deposited hundreds of km away from major sources of terrigenous input and provide relatively indirect evidence for changes in sea-level and sedimentary input. In addition, these sites contain few, weathered, and relatively poorly preserved carbonate macrofossils (bivalves and belemnites) that limit inorganic geochemical investigations.

In this study, we present new litho-, bio- and chemostratigraphic data from various bivalve-rich siliciclastic successions in the Vilyui River Basin that were deposited in a proximal position along the Anabar Shield close to the North Pole during the Early Jurassic (Lutikov, 2024). The new data are used to correlate the studied successions with coeval similar records from lower latitudes. Our findings provide insight into the spatiotemporal variability in climate conditions, sediment dynamics, and bottom water oxygenation in nearshore polar marine settings during this critical interval of Earth's history.

2. Geological setting

During the summer of 2021, five sections (2a, 3a–b, 4a–d, 5a, 7a) were measured and sampled along the Vilyui River, specifically between Kuokunu and Suntar in the Republic of Sakha, East Siberia, Russian Federation (Fig. 1 and Fig. 2). This area was situated near the North Pole during the Early Jurassic (Golonka, 2011; Torsvik et al., 2012; van Hinsbergen et al., 2015; Sømme et al., 2018; Fig. 1). The studied area is located in the western part of the Vilyui River Basin, a Mesoproterozoic to Mesozoic sedimentary basin characterized by a Late Devonian rifting phase (Polyansky et al., 2013). Jurassic sediments unconformably overlay Devonian-Carboniferous and Triassic deposits, with a total Jurassic–Cretaceous cover of less than one kilometre thick in the sampling area, located above the Suntar structural high (Polyansky et al., 2013).

The studied sections span the upper Ukugut Formation (Fm) (?Hettangian–lower Pliensbachian), the Tyung Fm (upper Pliensbachian) and the Suntar Fm (Toarcian). They extend up to the base of the Yakutsk Fm (lower Aalenian; Fig. 2; supplementary Figs. S1-S2). These formations have been previously studied in the more distal part of the basin along the Vilyui tributaries (Tyung, Markha, and Sinyaya rivers) (Koshelkina, 1961; Kirina, 1961; Knjazev et al., 1991). The Ukugut Fm consists mainly of cross-bedded sand and conglomerate beds deposited in alluvial to deltaic environments (Zverkov et al., 2021; Frolov et al., 2024). The age of this formation is upper Sinemurian to lower Pliensbachian as determined by its pollen assemblage (Goryacheva, 2017).

The overlying Tyung Fm is composed of silt, sand, and sandstone beds that were deposited in a proximal marine environment (Knyazev et al., 1991). The Tyung Fm is attributed to the upper Pliensbachian, as indicated by presence of the unfigured ammonite *Amaltheus margaritatus* in this formation near section 2a (Koshelkina, 1961), along with its microfossil assemblages, which include dinoflagellate cysts *Nannoceratopsis deflandrei* (Goryacheva, 2017). It should be noted that the precise position of the *Amaltheus* found in this section is controversial, in our opinion. It was found in Member III. Due to the scarce occurrence of ammonites, biostratigraphic subdivision of the formation is based on bivalve assemblage (Lutikov and Arp, 2023). Member III features coarsening-upward, cross-bedded sandstone beds containing isolated gravel and pebbles of variable size, as well as common glendonites, showing increasing size trend upsection throughout the entire basin (Rogov et al., 2023a). The topmost part of the Tyung Fm and basal surface of the Suntar Fm in sections 7a and 4a contain poorly preserved belemnite rostra that may represent some of the oldest records of the mass migration of this group in Arctic seas (Rogov et al., 2023b).

The Suntar Fm consists of clay, siltstone, and sandstone beds deposited in a shallow marine setting (Knjazev et al., 1991). The formation shows a general upward coarsening trend and is characterized by common erosional surfaces and clayey-calcareous concretions (Knjazev et al., 1991). The Suntar Fm lies unconformably on the Tyung Fm, marking both erosion of the Tyung Fm and a regional westward transgression in the early Toarcian (Devyatov et al., 2011). This contact is overlain by thin, organic-rich laminated clay beds that yielded poorly preserved bivalves and belemnite rostra near the base of the formation as well as a coleoid jaws (Rogov et al., 2023b). A single specimen of the Toarcian ammonite genus *Cleviceras* cf. *exaratum* (Young et Bird) was found about 1 m above its base near section 2a (Rogov et al., 2023b). It was previously figured as *Paltarpites argutus* (Koshelkina, 1961; Fig. 3) and later re-identified as *Harpoceras* cf. *exaratum* (Mesezhnikov, 1966), a determination subsequently confirmed by N. G. Krimholz and Yu. S. Repin (oral communication). Although Koshelkina (1961) reported it

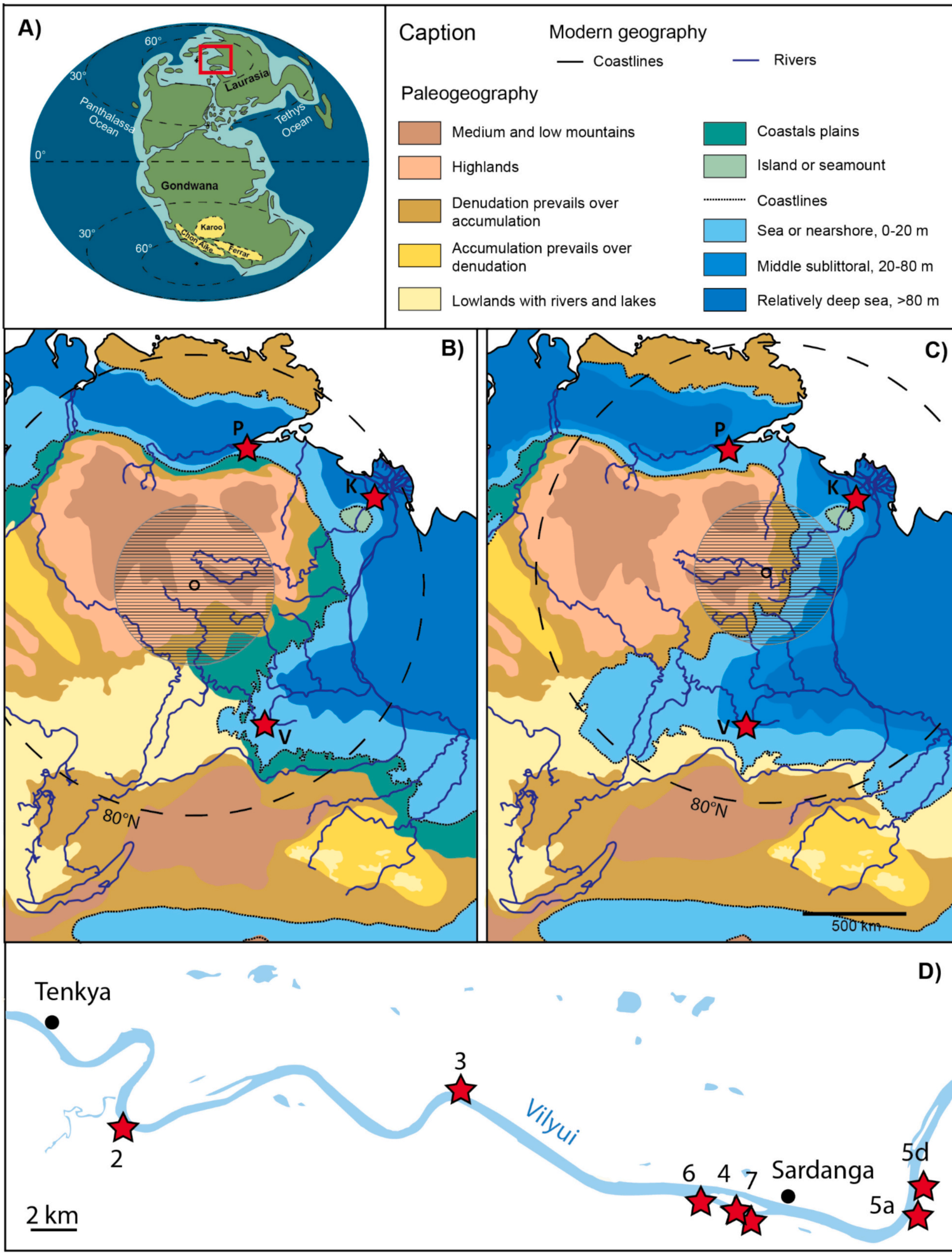

Fig. 1. Paleogeographic position of the studied sites and other Siberian sites discussed in the text. A) Early Toarcian global paleogeographic map (modified after Dera et al., 2009); B) and C) paleogeography of the Vilyui River Basin and the Anabar Shield region during the Late Pliensbachian and Early Toarcian, respectively (modified after Devyatov et al., 2011). V: Vilyui River (this study, Rogov et al., 2023b), K, Kelymiar River, P: Polovinnaya River (Suan et al., 2011; Letulle et al., 2022); D) Position of the studied sites along the studied segment of the Vilyui River (modified after Rogov et al., 2023b). The panels B and C show the position of the paleo North Pole (circles) with uncertainty (shaded areas) estimated for the paleomagnetic reference-frame of Torsvik et al., (2012), van Hinsbergen et al. (2015) and Vaes et al. (2023).

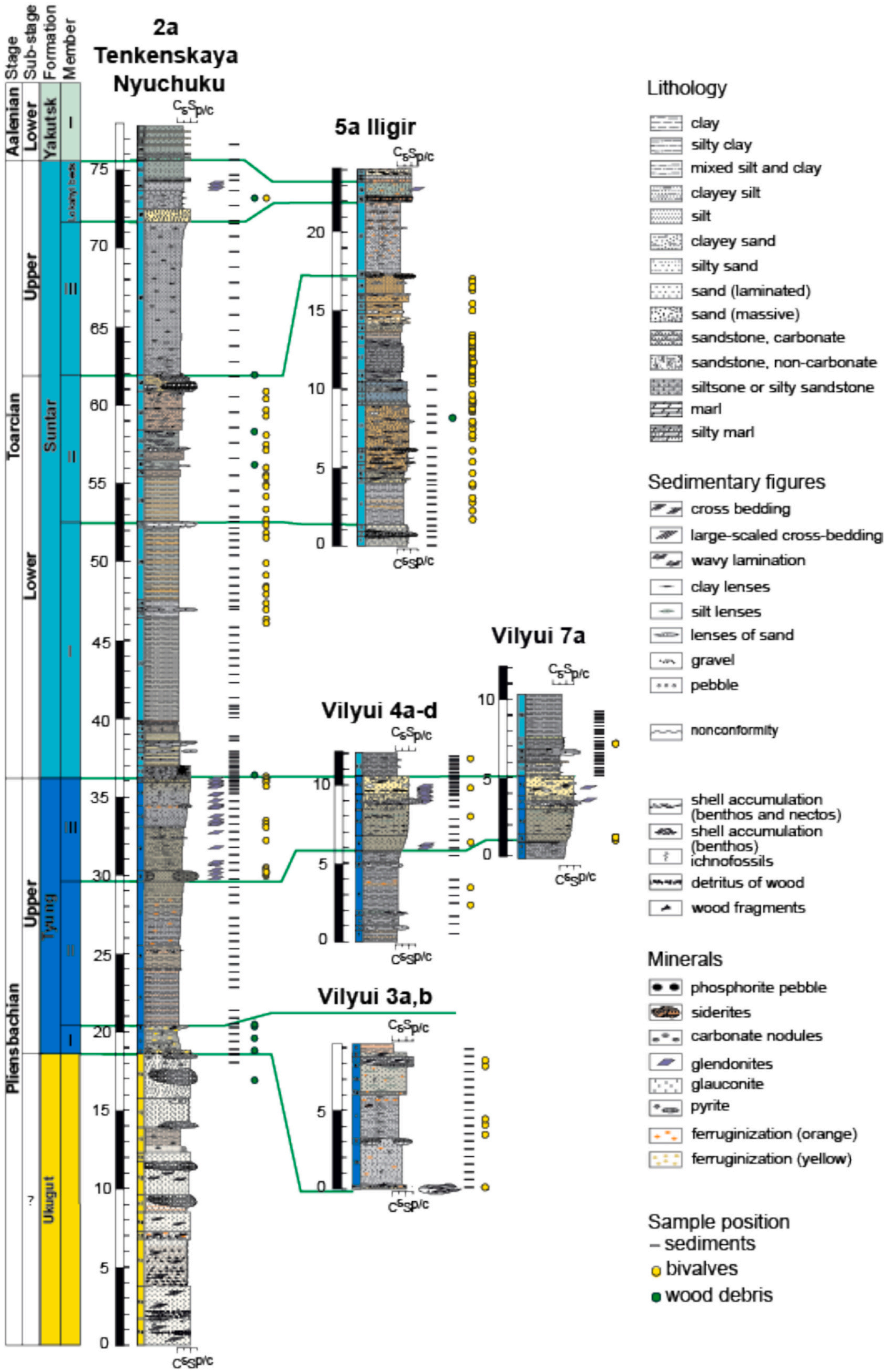

Fig. 2. Stratigraphic logs and sample positions of the measured section of the Vilyui River. The green correlation lines are based on litho- and biostratigraphy (see supplementary Fig. S1 for the detailed litho- and bio-stratigraphic subdivisions). (For interpretation of the references to colour in this figure legend, the reader is referred to the web version of this article.)

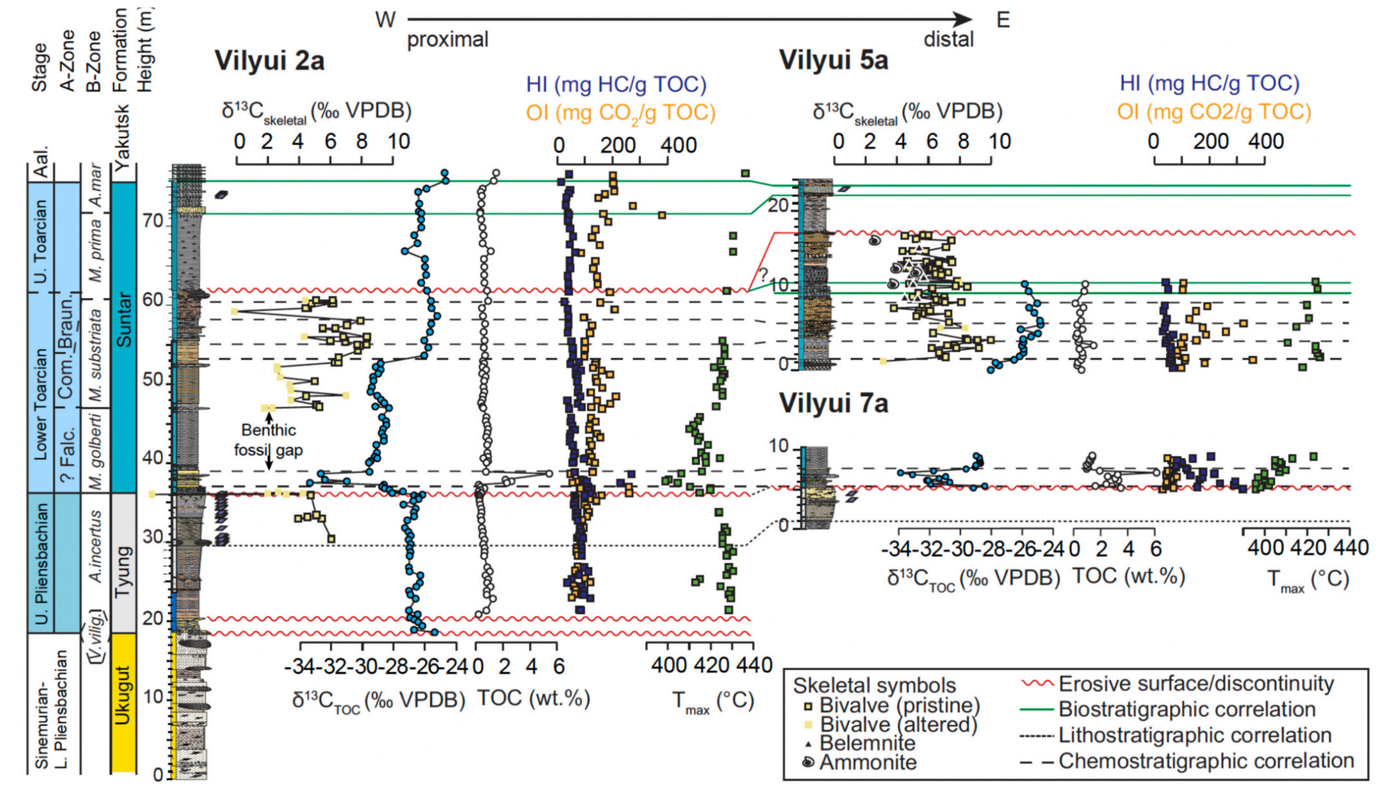

Fig. 3. Geochemical and Rock-Eval pyrolysis data from the Lower-Middle Jurassic of the Vilyui River Basin. The correlation between the three sections shown in Fig. 2 was refined by combining the available bio- litho- and chemo-stratigraphic constraints. Note that 7 m represented between 11 and 17.3 m at Vilyui 5a were eroded or non-deposited at Vilyui 2a. Dots with dashed lines correspond to bivalve samples that have low $\delta^{13}C$-$\delta^{18}O$ values that suggest diagenetic impact. A-Zone = ammonite Zone; B-Zone = bivalve Zone; Ant.–Falc. = Antiquum–Falciferum; Margar. = Margaritatus; vil.? = Viligensis?.

from a thicker bed, our conclusion is based on the preserved matrix rock for this specimen. The basal part of the Toarcian is either significantly thinner or absent in the Suntar Fm. The Pliensbachian–Toarcian boundary as defined by the GSSP (Rocha et al., 2016), could then fall either within the hiatus or into the uppermost part of the Tyung Fm.

The silt and sand beds of the middle Suntar Fm (Member II) did not yield ammonites in section 2a. In the eastern part of the studied area (near Illigir; section 5a), these levels contain common ammonites of early Toarcian age (*Dactylioceras*, *Harpoceras,* and *Zugodactylites*; Dagis, 1974), as well as bivalve accumulations (mostly belonging to *Dacryomya* and *Tancredia*) and belemnites (Lutikov and Arp, 2023; Rogov et al., 2023b). The species *Dactylioceras (D.) commune* (index species of the Commune Subzone in both the Boreal and Standard schemes) and *Dactylioceras* (*Microdactylites*) cf. *suntarense* Krimholz were reported in section 5a (Knyazev et al., 2003; their section 19). Fossil molluscs are less common in the silty sand beds of the upper part of the Suntar Fm, with a single occurrence of the ammonite genus *Pseudolioceras* reported in the more distal sections of the Markha River, suggesting an upper Toarcian age (Knyazev et al., 2003; Lutikov and Arp, 2023). The Suntar Fm is overlain by sand beds of the Yakutsk Fm, which are represented by only a few meters in the measured sections 2a and 5a and have been tentatively dated as Aalenian in age (Goryacheva, 2017).

3. Material and methods

3.1. Whole-rock sample preparation

Unweathered samples used for Rock-Eval pyrolysis (n = 131) and organic carbon isotopes (n = 135) were dried at 45 °C. Approximately 5 g of whole-rock powder was then obtained using an agate mortar at the Institute of Earth Sciences (ISTE, University of Lausanne) and at the Laboratoire de Géologie de Lyon, Terre-Planètes-Environnement (LGL-TPE, Université Lyon 1).

3.2. Rock-Eval pyrolysis

A total of 131 powdered whole-rock samples from sections 2a (n = 93), 5a (n = 20), and 7a (n = 18) were analyzed using a Rock-Eval 6 pyrolyzer (Vinci Technologies) at the ISTE to assess kerogen types and maturity. The Rock Eval 6 data include the total organic carbon (TOC, in wt%) content, mineral carbon (MinC, in wt%), hydrogen index (HI, in mg HC/g TOC), oxygen index (OI, in mg CO_2/g TOC), and T_{max} values (°C) being the temperature at which maximum cracking of kerogen in a sample occurs. Samples were calibrated using the IFP160000 (Espitalié et al., 1985; Behar et al., 2001). The HI and OI values were only interpreted for TOC ≥0.2 wt%, and T_{max} values were rejected when $S_2 \leq 0.25$ mg HC/g, where S_2 peak measures the hydrocarbons released during thermal cracking of the organic matter), thereby avoiding the misinterpretation of flat thermograms (Peters, 1986).

3.3. Organic carbon isotopes of bulk sediment

The organic carbon stable isotope composition ($\delta^{13}C_{org}$) of 135 decarbonated (HCl, 10% treatment) whole-rock powdered samples was measured in sections 7a, 5a, and 2a. Samples from sections 7a (n = 19) and 5a (n = 20) were measured at the LGL-TPE and samples from the most continuous section 2a (n = 96) were measured at the Institute of Earth Surface Dynamics (IDYST, University of Lausanne). All samples were decarbonated prior to analysis using 1 to 4 g of powdered sediment that were reacted with 1 N HCl at room temperature overnight. The residue was centrifuged and rinsed with deionized water at least three times until neutrality was reached, and oven-dried at 40 °C. At the LGL-TPE, between 4 and 14 mg of decarbonated residue was weighed in tin capsules and placed in Elementar Vario MICRO Cube® elemental analyzer connected to a GV Isoprime® isotope-ratio mass spectrometer in continuous helium flow. The calibration and assessment of the reproducibility and accuracy of the isotopic analysis were based on replicate analysis of two international reference materials (IAEA-CH-6 and IAEA-600) and an acetanilide laboratory reference material (ACE) measured alongside the samples. The EA device provided total organic carbon contents of the carbonate-free residue (EA-TOC_{cf}) with a precision better than 0.1%. At the IDYST, 3 to 10 mg of decarbonated residue was weighed and placed in a Carlo Erba 1108 elemental analyzer connected to a Thermo Fisher Scientific Delta V Plus isotope-ratio mass spectrometer following Spangenberg (2024). The reproducibility and accuracy were better than ±0.1‰ $\delta^{13}C_{org}$ (1σ). The carbon isotope ratios are reported in the delta notation in per mil (‰) relative to the Vienna Pee Dee belemnite limestone standard (VPDB).

3.4. Mollusc shell preparation and sampling

About 143 mollusc shells from sections 2a (n = 50, only bivalves), 3a–b, 4a–d and 5a (n = 90, 77 bivalves, 9 belemnite rostra and 4 ammonites) were sampled for geochemical analyses (see sections 3.4 to 3.6). Mollusc shells are unevenly distributed stratigraphically and taxonomically (mainly bivalves, few belemnites, and ammonites) across the sections studied (Fig. 2, supplementary Fig. S1). The shells were all examined under a binocular microscope during sampling with stainless steel dental tools. After removal of the sediment and alteration crust covering their outer surface, the belemnite rostra were fragmented. The visually best-preserved fragments were selected under a binocular microscope, taking care to avoid the apex, the apical and outermost parts, which are more likely to be diagenetically altered (Ullmann et al., 2015), then ground to powder using an agate mortar and pestle. Prior to geochemical analyses, Raman spectra were collected for most samples using a XploRa Raman spectrometer mounted on an optical microscope at Université Lyon 1 to assess their mineralogy and verify whether bivalve shells – primarily composed of aragonite (i.e. *Dacryomya* and *Tancredia*; Letulle et al., 2022) – still preserved their original aragonite composition. Furthermore, selected representative fragments were examined using a Phenom Pure G2 scanning electron microscope (SEM) in backscatter electron (BSE) mode at Université Lyon 1 to evaluate the preservation of the shell microstructures and identify potential diagenetic features (e.g., dissolution, recrystallization), through comparison with modern bivalve microstructures (Bieler et al., 2014). Mollusc shells were studied for $\delta^{13}C_{carb}$, and a subset of the best-preserved samples with sufficient material distributed along the sections was selected for $\delta^{34}S_{CAS}$ (n = 23) and $^{87}Sr/^{86}Sr$ (n = 25) analyses. For the subset of samples measured for $\delta^{34}S_{CAS}$, concentrations of selected major and trace elements (e.g., Fe, Mn), along with SO_4 content, were also measured to provide additional constraints on shell preservation.

3.5. Carbonate carbon stable isotopes on mollusc shells

Most calcium carbonate carbon stable isotope ratios ($\delta^{13}C_{carb}$) were measured on ~400 μg aliquots of the powdered shells at the LGL-TPE. Each sample was reacted with anhydrous oversaturated phosphoric acid at 90 °C for 20 min and released CO_2 purified by a MultiPrep™ autosampler. Derived CO_2 was transferred to the coupled dual-inlet then its isotopologue ratios (m/z = 44, 45 and 46) measured by a GV IsoPrime® isotope ratio mass spectrometer. All samples were analyzed in duplicate and the measured isotope ratios normalized to the VPDB scale using international reference materials NIST NBS18 ($\delta^{18}O_{VPDB}$ = −23.2‰; $\delta^{13}C_{VPDB}$ = −5.01‰), NBS19 ($\delta^{18}O_{VPDB}$ = −2.20‰; $\delta^{13}C_{VPDB}$ = +1.95‰), and a Carrara marble laboratory reference material ($\delta^{18}O_{VPDB}$ = −1.84‰; $\delta^{13}C_{VPDB}$ = +2.03‰) measured alongside the samples. Since 2019, the reproducibility of the Carrara Marble laboratory reference material has been ±0.096‰ for $\delta^{18}O$ (2σ, n = 1630) and ± 0.070‰ for $\delta^{13}C$ (2σ, n = 1630). These stable isotope data were complemented with $\delta^{13}C$ data obtained from clumped isotope measurements performed at the Laboratoire des Sciences du Climat et de l'Environnement (LSCE, Université Paris-Saclay), using the same analytical procedures described in (Letulle et al., 2022). Samples measured at both facilities showed very good interlaboratory reproducibility. The $\delta^{18}O$ and Δ_{47} values obtained on these same samples will be the subject of a dedicated study.

3.6. Carbonate-associated sulphate sulfur stable isotopes on mollusc shells

The sulfur isotope ratio ($^{34}S/^{32}S$) of carbonate-associated sulfate (CAS) was measured at the IRISS analytical platform (Isotopes Radiogéniques, Isotopes Stables, Salle blanche, CNRS, Nancy), following the procedures detailed by Paris et al. (2013). Briefly, 4 to 14 mg of powdered mollusc shells was dissolved in HCl. Sulfate concentration was measured using a Metrohm ion chromatography system. Sulphate was purified by anion exchange chromatography using 0.8 ml of AG-1-X8 Dowex resin (Paris, 2023). Sulfur isotopes of the purified aliquots were measured on a Thermo Scientific Neptune Plus™ Multi-collector inductively coupled plasma mass spectrometer (MC-ICP-MS) following Paris et al. (2013). The sulfur isotope ratio of the CAS ($\delta^{34}S_{CAS}$), measured against an in-house Na_2SO_4 bracketing standard solution calibrated against the IAEA S1 (Ding et al., 2001), is reported in ‰ against Vienna-Canyon Diablo Troilite (V-CDT). Analytical reproducibility (2σ) was estimated running Atlantic seawater through the protocol. The obtained mean value was 21.13‰ ± 0.14‰ (n = 3), in agreement with published values (eg. Paris, 2023). The blank was measured at $\delta^{34}S$ = 2.2 ± 2.4‰ (n = 3) and represents 0.4 nmol (± 50% Relative Standard Deviation), which is 4 to 6% for samples 103 S, 108 S biv, 132 S biv1, 18 S biv1, 51 S biv1 and less than 4% for the other samples). Measured values were corrected for the blank contribution.

3.7. Radiogenic Sr ratio of mollusc shells

All $^{87}Sr/^{86}Sr$ measurements of mollusc samples were carried out at the LGL-TPE following the procedures described by Guiserix et al. (2022). Briefly, 1 to 1.5 mg of carbonate sample powder was dissolved in 1 ml HNO_3 (3 M). The solution was dried and dissolved again in 0.3 ml HNO_3 (3 M). Sr was recovered after elution through a chromatographic column packed with Sr spec™ resin. The Sr solution was dried and dissolved in HNO_3 (0.05 M) before measurement by mass spectrometry. The calcium carbonate standard SRM-915b was prepared in parallel with the fossil samples. The solutions were measured for $^{87}Sr/^{86}Sr$ ratios on a Thermo Scientific Neptune Plus™ MC-ICP-MS at the LGL-TPE alongside a preparation of the standard SRM (NIST) 987. The obtained $^{87}Sr/^{86}Sr$ values were adjusted to a value of 0.710248 for SRM (NIST) 987 as reported in previous studies of this interval (McArthur et al., 2000, 2020). Reproducibility of SRM (NIST) 987 over the analytical session was ±0.00004 (2 σ; n = 30).

4. Results

4.1. Organic carbon isotopes

The $\delta^{13}C_{org}$ values in section 2a vary between −27.4 and − 25.4‰ in the Tyung Fm (Fig. 3). The $\delta^{13}C_{org}$ values show an abrupt 2‰ decline in the lowermost Toarcian (Suntar Fm, reaching minimal values (−33.4 to −31.0‰) in the clay-rich interval between 37 and 38.5 m. This is followed by an increase in $\delta^{13}C_{org}$ values, reaching −29.6‰ at 39 m. The $\delta^{13}C_{org}$ profile shows a gradual 1.5‰ increase up to 47 m followed by an interval of lower values (−28.6 to −29.5) between 47 and 53 m. The $\delta^{13}C_{org}$ values increase abruptly by 3‰ at 53.5 m and increase gradually to reach a maximum value of −25.2‰ at 58.6 m. This is followed by a steady decrease of 1‰ up to 72.8 m and an increase by >2‰ across the transition between the Suntar and Yakutsk fms.

The $\delta^{13}C_{org}$ values in section 7a range from −33.9 to −28.4‰ in the lowermost Toarcian (Suntar Fm) and record a > 5‰ n-CIE over 2.5 m of fine-grained sediments that tracks that of section 2a, although with a higher sample density. The $\delta^{13}C_{org}$ values in section 5a range from −24.8 to −28.0‰ and show a > 3‰ increase of $\delta^{13}C_{org}$ values between 0 and 5.7 m followed by a 1‰ decrease between 6 and 11 m, a pattern almost identical to that recorded in the middle part of the Suntar Fm at section 2a (Fig. 3).

4.2. Rock Eval pyrolysis

The TOC values in sections 2a, 5a, 7a range from 0.1 to 6.1 wt%, with the highest values recorded in the lowermost Toarcian (Suntar Fm). The most continuous TOC profile at section 2a generally shows maximum TOC values in fine-grained beds and minimal values in sand-rich beds (Fig. 3). For all sections, HI and OI values vary between 12 and 326 mg HC/g TOC and 33–76 mg CO_2/g TOC, respectively (Fig. 3). The TOC-rich samples from the lowermost Toarcian (basal Suntar Fm) record the highest HI values, and the highest OI values generally corresponding to sand-rich beds (36.0–37.25 m; 59.6 m; 71.6 m).

The T_{max} values range from 398 to 437 °C, with a median value of 425 °C in section 2a (Fig. 3). The T_{max} profiles show several decreases of >10 °C that are coeval in the three sections and respectively recorded at 25, 38, 44, 56 and 60 m in section 2a, 5 m in section 7a, 4 and 9 m in section 5a.

4.3. Mollusc shell preservation

Most mollusc samples revealed an excellent preservation of their microstructures. Raman spectra and SEM-observed microstructures are consistent with original aragonite for most of the analyzed samples (*Dacryomya, Tancredia, Panope, Preameleagrinella*), or pristine foliated calcite (*Liostrea, Harpax*) (Supplementary Fig. S4). Two samples of *Harpax* (section 3a–b and 4a–d) yielded mixed calcite and aragonite mineralogy in Raman spectra. These specimens exhibit a thin, fibrous, white and iridescent outer layer – almost absent in other specimens – clearly distinct from the inner layer composed of foliated calcite. This shell structure most likely reflects a combination of a calcite and aragonite mineralogy, which is a common feature reported in plicatulid bivalves (Hautmann, 2006). Aragonite bivalves appear chalky on the outer shell, sometimes greasy in carbonate concretions, with dendritic oxides at the sediment-shell interface. Secondary calcite infilling occurred in some concretions. Among the 11 studied bivalve specimens from the upper Tyung Fm. of Vilyui 2a, 5 showed signs of partial recrystallization. In the Suntar Fm, the two most common bivalve genera *Tancredia* and *Dacryomya* are associated with different preservation, probably related to their different microstructures. The acicular aragonite shells of *T. bicarinata* are usually dull up to ~0.5 mm below the shell surface, sometimes porous with a yellowish colour, and show a massive structure when fractured. The shells of *D. jacutica* are dull only in their outermost part corresponding to their outer prismatic layer. They are brittle and fracture along the planes of their sheet nacreous microstructure, showing iridescent surfaces. We found evidence of partial recrystallization in the form of rhombohedral calcite microcrystal or mixed aragonite-calcite Raman spectra on eleven originally aragonitic bivalve specimens.

Belemnite rostra occur in the upper part of Member II of the Suntar Fm in section 5a. Their surface is covered by sediments or a thin alteration crust. They show a clear radial crystalline structure of elongated fibrous prism with concentric growth lines and a hollow and dull apical area of spherulitic calcite. Ammonite shell fragments are found in carbonate concretions and silty clays in the uppermost part of Member II of the Suntar Fm in section 5a, and are all greasy with crystallised fractures. The subset of samples measured for trace element concentrations ($n = 23$) yielded Fe contents below 1 ppm in all cases. Mn concentrations were generally below 500 ppm, with the exception of one sample exceeding 1500 ppm.

4.4. Carbonate carbon stable isotopes

The $\delta^{13}C_{skeletal}$ values of the two *Harpax* shells from the Tyung Fm in section 3a-b and 4a–d show a decrease from 5.5 to 4.0‰ between Member I and II. The $\delta^{13}C_{skeletal}$ values measured on the 11 aragonite bivalves of the glendonite-bearing strata of Tyung Fm member III in section 2/1a range from −5.4 to 6.0‰ (Fig. 3). The aragonite bivalves from the upper part of the Suntar Fm member I in section 2/1a, yield $\delta^{13}C_{skeletal}$ values ranging from 1.8 to 5.1‰. The Suntar Fm member II has a denser geochemical coverage owing to its fossil richness. In section 2a, the bivalve $\delta^{13}C_{skeletal}$ values increase markedly above 52 m to around 7.8‰ reaching up to 8.3‰. In the following 3 m $\delta^{13}C_{skeletal}$ values are scattered from 5.5 to 8.3‰ and decrease in the uppermost levels of the member where they range from 4.4 to 6.1‰.

The $\delta^{13}C_{skeletal}$ profile in section 5a shows similar trends as those observed in section 2a, with values increasing from 7.1 to 9.0 and up to 10.0‰ at 2.5 m and decrease to values of 5.5‰ in the following 4 m and remain relatively stable but scattered from 4.2 to 8.5‰ up section (Fig. 3). The $\delta^{13}C$ values of belemnites, ranging between 4.5 and 6.1‰, overlap with the lower range of $\delta^{13}C$ values measured in co-occurring bivalves, and show no clear stratigraphic trends. The ammonites yielded much lower $\delta^{13}C$ values ranging between 2.6 and 5.3‰ (Fig. 3).

The skeletal oxygen isotope data are reported in Table S2. Their thermal/hydrological significance will be discussed in a dedicated study, and hence not discussed further in this (mostly) chemostratigraphic study.

4.5. Carbonate-associated sulphate sulfur stable isotopes

The $\delta^{34}S_{CAS}$ values were measured on a subset of 23 specimens of exclusively aragonitic bivalve shells, except for Member II of the Tyung Fm where no fully aragonitic bivalve had been recovered. The $\delta^{34}S_{CAS}$ values range from 1.4 to 22.6‰ (n = 23). The *Harpax* calcite from member II of Tyung Fm (section 4a–d) yielded a $\delta^{34}S_{CAS}$ value of 13.3‰ (Fig. 4). The $\delta^{34}S_{CAS}$ signal is noisy in the upper Tyung Fm of section 2a (7.0 to 17.5‰; $n = 3$; Fig. 4), and in Member I of the Suntar Fm (7.2 to 16.0‰; $n = 4$; Fig. 4). Apart from one outlier, bivalve $\delta^{34}S_{CAS}$ values increase in the Suntar Fm Member II of section 2a from 15.9 to 20.4‰ (n = 4; Fig. 4), a trend confirmed in section 5a with more stable values around ~20‰ (18.7 to 22.6‰; $n = 10$; Fig. 4).

4.6. Radiogenic Sr ratio

The $^{87}Sr/^{86}Sr$ ratios range from 0.70698 ± 0.00004 to 0.70734 ± 0.00004. The values recorded in the calcitic part of two *Harpax* specimens from the lower and middle part of the Tyung Fm (section 3a–b and section 4a–d) range from 0.70698 to 0.70714 (Fig. 4). Two aragonitic bivalves from the glendonite-rich beds in section 2a yielded $^{87}Sr/^{86}Sr$ ratios of 0.70708 ± 0.00004 and 0.70720 ± 0.00004. The $^{87}Sr/^{86}Sr$ ratios of aragonitic bivalves in the middle part of the Suntar Fm in section 2a are around 0.70727 ± 0.00003 (2 SD, n = 4), apart from one sample with a lower $^{87}Sr/^{86}Sr$ ratio (0.70712 ± 0.00004; Fig. 4) that also records anomalous $\delta^{13}C$-$\delta^{18}O$ values and is hence very likely diagenetically altered.

Most of the samples in the section 5a show values in the same range as in section 2a (~0.70727), with few samples with lower $^{87}Sr/^{86}Sr$ ratios in the upper part of the section, including the calcitic ostreid *Liostrea* that yields the lowest $^{87}Sr/^{86}Sr$ ratio of the lower Toarcian dataset (0.70706 ± 0.00004; Fig. 4). In this interval belemnite rostra have a lower variability in $^{87}Sr/^{86}Sr$ ratios (mean = 0.70729 ± 0.00002; 2SD, $n = 5$) than aragonitic bivalves (mean = 0.70724 ± 0.00007; 2SD, $n = 9$), but the $^{87}Sr/^{86}Sr$ difference between belemnite rostra and aragonitic bivalves from the same level shows no significant systematic offset (mean offset = 0.000066 ± 0.000074; 2 standard error of the mean, n = 5).

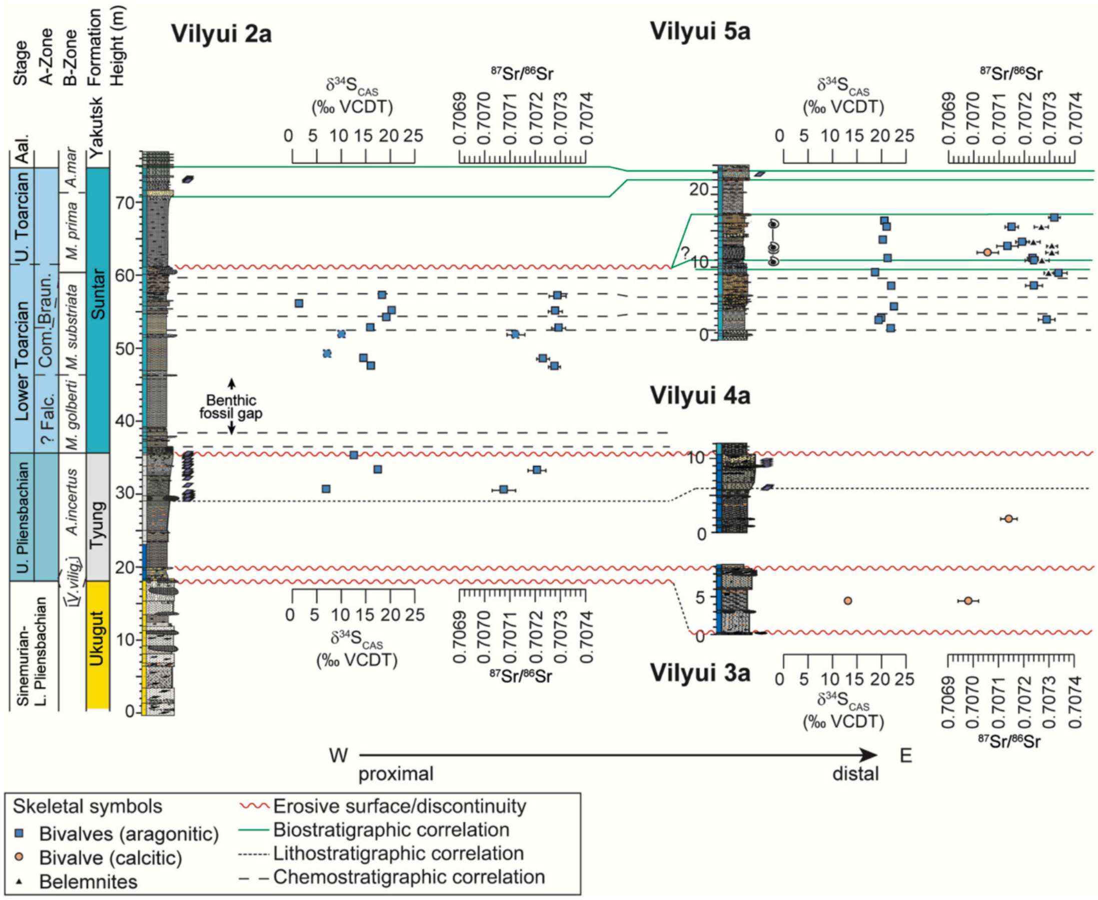

Fig. 4. Sulfur and strontium isotope data from the Lower-Middle Jurassic of the Vilyui River Basin. The correlations between sections 2a, 3a–b, 4a–d and 5a are based on Figs. 2 and 3. Dots with dashed lines correspond to bivalve samples that have low $\delta^{13}C$-$\delta^{18}O$ values that suggest diagenetic impact.

5. Discussion

5.1. Source and preservation of the organic matter

Organic matter (OM) content is relatively low throughout the Pliensbachian–Toarcian interval at Vilyui River and mostly of terrestrial origin, as suggested by generally low HI and OI values, typical of Type III kerogen (Fig. 3). The adjacent landmasses (Fig. 1) might have been the source of terrestrial OM in the Vilyui Basin. In contrast to most of other coeval sites from lower latitudes, TOC and HI are relatively low, suggesting that marine organic productivity was low and/or that preservation of algal/bacterial-derived OM was low due to oxygenated conditions at the water-sediment interface and/or sediment dynamics (see section 5.4 and 5.5). The marked increase in TOC contents and HI values in the earliest Toarcian (basal Suntar Fm) indicate a higher contribution of hydrogen-rich aquatic organic matter (Type II kerogen) and/or better preservation.

5.2. Representativeness of the carbon isotope profiles

An important prerequisite for the use of $\delta^{13}C$ profiles as a stratigraphic tool is that the potential compositional and diagenetic biases affecting the isotopic values can be identified and accounted for. Previous work on Lower Jurassic strata deposited at lower paleo-latitudes has shown that changes in the main proportion of OM types may have a major influence on the $\delta^{13}C_{org}$ profiles, with marine phytoplanktonic hydrogen-rich OM showing a 3–4‰ depletion in ^{13}C compared to the terrestrial one (Suan et al., 2015; Ruebsam et al., 2018; Chen et al., 2021). This influence in the studied samples from Vilyui is indicated by a moderately strong negative linear correlation ($R^2 = 0.47$; $p = 3.6E\text{-}19$; $n = 127$) between the measured $\delta^{13}C_{org}$ and HI values (a proxy for the hydrogen-rich aquatic kerogen content in the total organic fraction) in the three studied sections (Fig. 5). Interestingly, the HI- $\delta^{13}C_{org}$ intercept is similar to the one reported for other coeval sites (i.e., similar terrestrial endmembers) but the slope is much steeper, which suggests a more ^{13}C-depleted marine endmember. The observed HI-$\delta^{13}C_{org}$ relationships are consistent with modern phytoplanktonic $\delta^{13}C$ patterns at high latitudes (e.g., Rau et al., 1989) and suggest that aquatic OM in polar seas may have been substantially ^{13}C-depleted by several per mils relative to that from lower latitudes (e.g., Suan et al., 2011, 2015).

Following previous work (Suan et al., 2015), we assessed the possible corresponding compositional bias by using the observed $\delta^{13}C_{org}$-HI relationships to calculate changes in $\delta^{13}C$ values that are not explained by changing OM contribution. Regardless of the regression model we used, the reconstructed and measured organic $\delta^{13}C$ profiles are very similar (Fig. 5). In line with studies of lower latitude sites (Suan et al., 2015; Ruebsam et al., 2018; Chen et al., 2021), changes in OM source were thus most likely not the main driver of the recorded trends but instead they just reinforced it. It is worth mentioning that the measured and reconstructed organic $\delta^{13}C$ profiles show slight differences in their trend, notably in the magnitude of the carbon-isotope shifts. The n-CIE recorded within the lowermost Toarcian strata (basal Suntar Fm, 37.25–55.5 m) in the reconstructed profiles has a lower magnitude compared to the measured one and lacks the positive rebound seen between 40 and 49 m in the measured $\delta^{13}C_{org}$ profiles (Fig. 5).

Carbonate $\delta^{13}C$ profiles derived from mollusc (i.e., bivalves and belemnites) shells can be a valuable tool for reconstructing the paleoenvironmental conditions. However, the trends and magnitude of

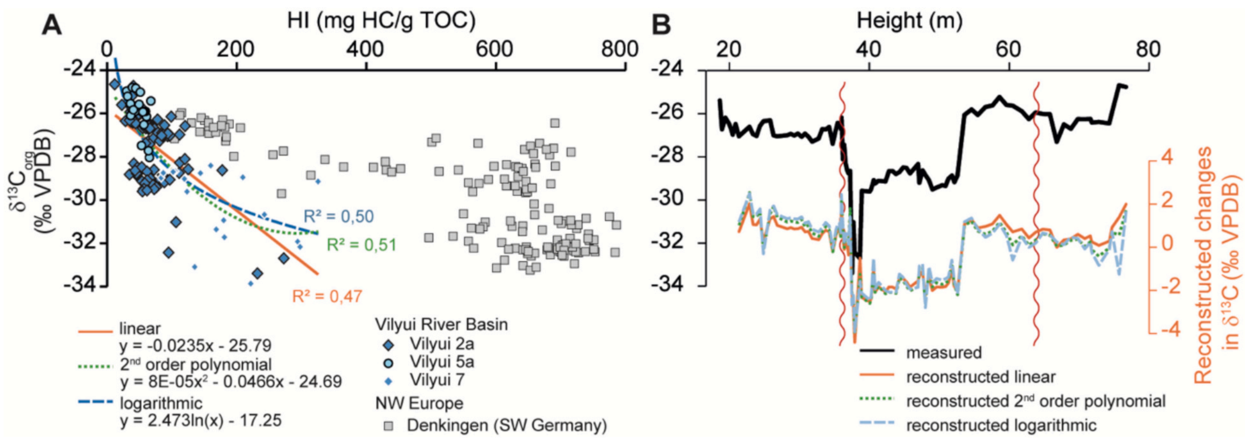

Fig. 5. A. Comparison of HI-$\delta^{13}C_{org}$ relationships in Pliensbachian–Toarcian sediment samples from the Vilyui River Basin (sections 2a, 5a, and 7a) and from Denkingen (Suan et al., 2015). The lines show the different regression models of all data-pairs from Vilyui River sections with the corresponding equations and correlation of determination; B. Comparison between measured and reconstructed $\delta^{13}C_{org}$ profiles for section 2a. The reconstructed profiles, computed using the regression models shown in A and the method described by Suan et al. (2015), correspond to changes in $\delta^{13}C_{org}$ values that are not explained by changes in HI values (i.e., changes in the proportion of aquatic versus terrestrial organic matter).

inorganic $\delta^{13}C$ values may be influenced by several factors, including metabolic activity of the mollusc species, the mineralogy of the carbonate, the preservation state of the shells, and the environmental characteristics of their habitat, such as water chemistry, salinity,

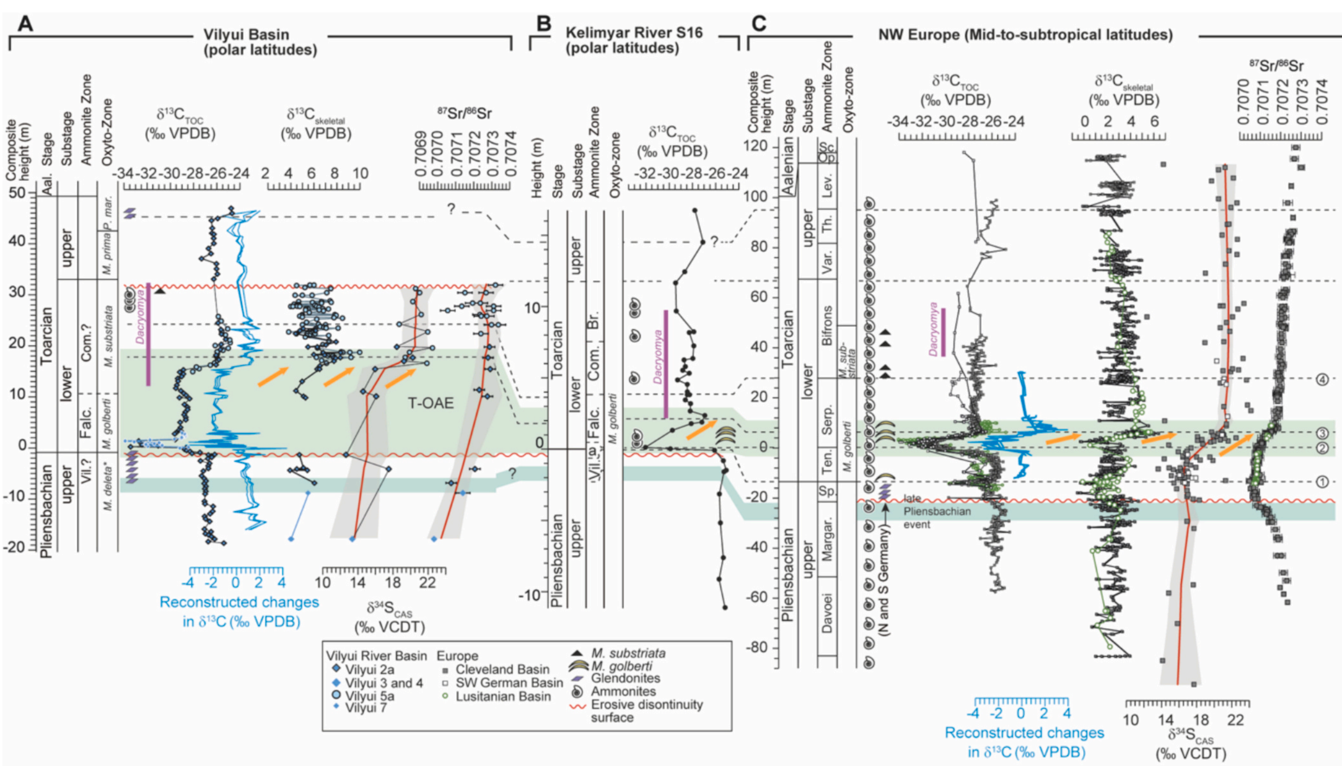

Fig. 6. Integrated stratigraphical correlations of the studied sections of Vilyui River Basin (A) with Pliensbachian-Toarcian sites of Siberia (B) (Suan et al., 2011) and Europe (C). The European $\delta^{13}C_{org}$ (Cohen et al., 2004; Suan et al., 2015; Fantasia et al., 2019; Jenkyns et al., 2001; Trabucho-Alexandre et al., 2022; van de Schootbrugge et al., 2020), $\delta^{13}C_{skeletal}$ (Ferreira et al., 2019; Korte et al., 2015; McArthur et al., 2000; Suan et al., 2010, 2008; Ullmann et al., 2014), reconstructed changes in $\delta^{13}C$ (Suan et al., 2015), $\delta^{34}S_{CAS}$ (Gill et al., 2011; Newton et al., 2011), and $^{87}Sr/^{86}Sr$ data (Jones et al., 1994a, 1994b; McArthur et al., 2000, 2020) have been projected against a composite height based on Yorkshire coast exposures. Also plotted are oxytomid bivalve Zone (Oxyto-zones) and positions of key index bivalve species from Vilyui River (this study), Kelimyar River (Lutikov, 2024; Lutikov and Arp, 2023) and Europe (Ludwigskanal); the European *Dacryomya* occurrence are from the Cleveland Basin (Caswell and Dawn, 2019). The European range of glendonites is based on N and S German sites (Merkel and Munnecke, 2023; Teichert and Luppold, 2013). The $\delta^{13}C_{org}$ data from Portugal (Fantasia et al., 2019) have been shifted by −3‰ to compensate for terrestrial organic matter influence and facilitate reading. The red lines in the $^{87}Sr/^{86}Sr$ and $\delta^{34}S_{CAS}$ data are 50% LOESS-smoothed profiles with 95% confidence intervals (gray envelopes). Correlation lines: 1 = Pliensbachian-Toarcian boundary; 2 = base of the n-CIE; 3 = top of the n-CIE; 4 = Serpentinum-Bifrons boundary Abbreviations: A. = Antiquum; Braun. = Braunianus; Com. = Commune Falc. = Falciferum; Lev. = Levesquei; Op. = Opalinum; Marg. = Margaritatus; Sc. = Scissum; Serp. = Serpentinum; Sp. = Spinatum; Ten. = Tenuicostatum; Th. Thouarsense; Var. = Variabilis; Vil. = Viligaensis;. (For interpretation of the references to colour in this figure legend, the reader is referred to the web version of this article.)

temperature, and local carbon sources. In addition to the Raman and microstructural criteria listed above, we have assessed the preservation of the material using inorganic $\delta^{13}C_{skeletal}$-$\delta^{18}O_{skeletal}$ crossplots including both skeletal samples and diagenetic cements (Fig. S5). This plot shows that 14 of the investigated bivalve samples have anomalously low $\delta^{13}C_{skeletal}$-$\delta^{18}O_{skeletal}$ values that clearly plot on a diagenetic mixing line, most of them with other evidence for alteration (section 4.3), and thus samples were excluded for further interpretation. We also note that the highest $\delta^{13}C_{skeletal}$ absolute values (commonly >6‰; up to 10.0‰) measured on the Toarcian aragonitic bivalves from the Vilyui River sections are higher than the maximal values (4–6‰) reported so far from Toarcian brachiopod and belemnite calcite (Fig. 6). Such differences might be due to the respective mineralogy of the measured molluscs, as observed in the aragonite of modern molluscs with mixed calcite-aragonite mineralogy, enriched by 1–2‰ relative to calcite (Lécuyer et al., 2012). In addition, it is not excluded that temperature gradients might have influenced the aragonite $\delta^{13}C$ values of the bivalves recorded at Vilyui. Grossman and Ku (1986) also reported an inverse correlation between aragonite ^{13}C fractionation relative to dissolved inorganic carbon and temperature in some modern benthic foraminifera and molluscs, with a decrease of 10 °C corresponding to an increase of 1.3‰ in the studied molluscs, a feature similarly observed on abiogenic carbonates (Romanek et al., 1992). Temperature gradients between the Tethyan and polar seas have been recently estimated to be within 10 to 20 °C (Letulle et al., 2022). The anomalously high aragonite $\delta^{13}C_{skeletal}$ values recorded at Vilyui relative to Tethyan values may thus be partly or entirely explained by a combination of thermal and mineralogical isotopic fractionation effects.

5.3. Reliability of the sulfur and strontium isotope profiles

Based on the mollusc $\delta^{13}C_{skeletal}$-$\delta^{18}O_{skeletal}$ diagenetic trend (section 5.2, Table S2), two $\delta^{34}S_{CAS}$ and seven $^{87}Sr/^{86}Sr$ data points are excluded from further interpretation. This criterion notably excludes the lowest $\delta^{34}S_{CAS}$ values and narrows the range of the dataset (12.6 to 22.6‰; $n = 19$). Trace element data (Fe and Mn) did not allow identification of additional altered samples. The low Fe contents (<1 ppm) are consistent with good preservation, while elevated Mn concentrations show no correlation with isotopic values ($\delta^{13}C_{skeletal}$, $\delta^{18}O_{skeletal}$, $\delta^{34}S_{CAS}$ or $^{87}Sr/^{86}Sr$; Table S2). CAS in biogenic carbonates are regularly used to reconstruct seawater $\delta^{34}S$, mostly using foraminifera and brachiopods (Paris et al., 2014; Present et al., 2015; Rennie et al., 2018; Thaler et al., 2023). However, the $\delta^{34}S$ signal may be influenced by metabolic effects of the bivalves that can generate deviations from seawater toward lower $\delta^{34}S$ values (Bryant et al., 2023). While local environmental factors, such as freshwater influx or mixing processes that could modify the sulphate pool, may also produce such negative shifts, these influences are considered unlikely here given the overall consistency of the $\delta^{34}S$ record with open-marine conditions. Thus, we infer that the locally lower values not explained by diagenesis most likely reflect mollusc-specific vital effects. All belemnite $^{87}Sr/^{86}Sr$ ratios, all belonging to the Commune Subzone (Fig. 4), are excluded as their $\delta^{18}O_{skeletal}$ values (Table S2) and their microstructural aspect suggest diagenetic overprinting. This is supported by their high $^{87}Sr/^{86}Sr$ ratios (mean: 0.70728 ± 0.00003; 2 SE; $n = 6$) relative to Tethyan belemnites (mean: 0.70720 ± 0.000002; 2 SE; $n = 11$) (McArthur et al., 2000, 2020). Nevertheless, Siberian belemnite $^{87}Sr/^{86}Sr$ ratios are not significantly different ($p_{same\ mean} > 0.05$) from those of well-preserved co-occurring bivalves (mean: 0.70721 ± 0.00008; 2 SE; $n = 8$), which could suggest a similar diagenetic history. Alternatively, the higher $^{87}Sr/^{86}Sr$ ratios recorded in belemnites from the Vilyui Basin may reflect coastal inputs enriched in Sr (e.g., runoff or submarine groundwater discharge; Huang et al., 2011; El Meknassi et al., 2018) derived from the Siberian craton and its sediments. This may also indicate enhanced regional weathering associated with the early Toarcian warming (Brazier et al., 2015; Dera et al., 2009; Yang et al., 2024), which contributed to the global rise in seawater $^{87}Sr/^{86}Sr$ ratios (Jones, 2001; McArthur et al., 2020, 2000).

Bivalve $^{87}Sr/^{86}Sr$ ratios display a significantly greater scatter (psame variance <0.05) than those of belemnites within this interval. As suggested by El Meknassi et al. (2018), the isotopic scatter of bivalve data most likely reflects their larger salinity tolerance relative to cephalopods, as well as their different ecology (benthic vs nectonic). As previously shown, the lower Toarcian *Dacryomya* bivalves record significant freshwater input in these Arctic regions (Letulle et al., 2022). This wider salinity tolerance makes bivalve shells less reliable archives of open marine $^{87}Sr/^{86}Sr$ ratios (El Meknassi et al., 2018) and weakens their use for $^{87}Sr/^{86}Sr$ chemostratigraphy. Nevertheless, the fossil assemblage of Vilyui River sections – including echinoderms and cephalopods – and the relatively limited dispersion of bivalve $^{87}Sr/^{86}Sr$ ratios (SD = 0.0001; n = 8) within the Commune Subzone suggest an open depositional setting, such as open coast or a proximal delta (El Meknassi et al., 2018), where 87Sr/86Sr values would be expected to deviate only slightly from open-marine conditions. All things considered, despite a slight offset relative to other $^{87}Sr/^{86}Sr$ ratios (8 ± 5 × 10–5) and the use of bivalves as the primary archive, our record remains in good agreement with established Pliensbachian–Toarcian seawater $^{87}Sr/^{86}Sr$ trends and can be confidently used for stratigraphic correlation of this polar record.

5.4. Correlation with coeval Pliensbachian–Toarcian records and implications

The studied sections at Vilyui River were correlated to existing coeval records from Siberia and Europe by means of biostratigraphy and chemostratigraphy (Fig. 6). Studied sections from Vilyui River were first assembled into a composite record using litho-, bio-, and chemostratigraphic constraints. Based on bivalve biostratigraphy, the base of the composite record is assigned to an upper Pliensbachian age (Fig. 6). Correlation based on carbon isotope stratigraphy of the upper Pliensbachian strata of Vilyui River with European sites is not straightforward. Notably, the late Pliensbachian event that is associated with a global carbon cycle perturbation and expressed as a positive carbon isotope excursion at worldwide distributed sites (e.g., Hollaar et al., 2023) is difficult to unambiguously identify at Vilyui River. However, $^{87}Sr/^{86}Sr$ profile in the upper Pliensbachian (Tyung Fm) at Vilyui River (mean = 0.7071 ± 0.0001; $n = 4$, 2 SEM) shows a range of values typical of the upper Pliensbachian in coeval sites from Europe (Jones et al., 1994a,b; McArthur et al., 2000, 2020). In addition, $^{87}Sr/^{86}Sr$ values <0.7071 recorded in the uppermost part of the Tyung Fm, have been similarly reported from European sites and solely from upper Pliensbachian–lowermost Toarcian (Spinatum–Tenuicostatum ammonite zones) strata (Fig. 6). This evidence further supports the presence of strata encompassing the Pliensbachian–Toarcian transition at Vilyui River and allows comparison with other Siberian and NW European sites (Fig. 6).

The Vilyui River composite geochemical reveals a large >3‰ n-CIE in the earliest Toarcian (Antiquum–Falciferum ammonite zones) which can be correlated to the T-OAE n-CIE recorded across the *Tenuicostatum–Serpentinum* transition in biostratigraphically well-dated NW European sites (Jenkyns et al., 2001; Kemp et al., 2005; Suan et al., 2011; Fantasia et al., 2019). The Falciferum Ammonite Zone thus lies above an erosive surface in the studied Vilyui River sites, consistent with the stratigraphy of most coeval Siberian records (Knyazev et al., 2003; Devyatov et al., 2010; Suan et al., 2011; Lutikov, 2024). This unconformity, which is also a characteristic of many proximal sites in Europe (Mailliot et al., 2009; Bomou et al., 2021; Ruebsam et al., 2024), has been attributed to an episode of short-lived subaerial exposure and erosion, due to a pronounced eustatic sea-level fall immediately predating the Toarcian hyperthermal.

At Vilyui River, the T-OAE n-CIE is followed by a positive 4‰ shift recorded in both $\delta^{13}C_{org}$ and $\delta^{13}C_{skeletal}$ profiles that can be correlated with that recorded at Kelimyar (Falciferum Ammonite Zone) and in European sites (first half of the Serpentinum Ammonite Zone) (Fig. 6). In addition, the correlation is further supported by the occurrence of *Dactylioceras* ammonites (25.75–31.3 m; Fig. 6), in particular of *Dactylioceras* ex gr. *commune* (Knyazev et al., 2003), which would correspond to the Commune Subzone (basal Bifrons Zone) in the European Subboreal Province (Page, 2003). This is consistent with the presence of the bivalve *Montacuta substriata* in section 5a (30 m; Fig. 6), which has its last occurrence in the *Commune* subzone in Germany (Lutikov, 2024). This correlation is further supported by the observation that the rising limb of the T-OAE n-CIE at Vilyui River is associated with a marked shift in $\delta^{34}S_{CAS}$ values (up to 6‰). A similar shift, from ~16 to ~22‰ is recorded in belemnite and whole-rock samples from Germany, Yorkshire and Italy (Gill et al., 2011; Newton et al., 2011). This latter feature has been interpreted to reflect a global perturbation of the sulfur isotope cycle due to the massive burial of pyrite characterized by highly negative $\delta^{34}S$ pyrite values in euxinic conditions (Gill et al., 2011). In addition, the composite $^{87}Sr/^{86}Sr$ profile shows an increasing trend that is consistent with that reported in European sites (e.g., Jones et al., 1994a, 1994b; McArthur et al., 2000, 2020; Fig. 6). The oceans have a homogeneous $\delta^{34}S$ value due to the long residence time of sulfate ions in seawater (≈ 10 My), and this property is likely to have held true throughout the Phanerozoic (Paytan et al., 1998; Paris et al., 2013; Tostevin et al., 2014; Rennie et al., 2018), the $\delta^{34}S$ record could be used to establish stratigraphic correlation. It has been suggested that ocean sulphate concentrations may have decreased during this interval, potentially enhancing the influence of local and regional processes on $\delta^{34}S_{CAS}$ (Newton et al., 2011; Han et al., 2023), particularly in shallow, proximal settings such as the one studied here, where runoff may have been significant. However, this influence appears minimal, given the close agreement between the Vilyui River $\delta^{34}S_{CAS}$ record and those from the western Tethys (Gill et al., 2011; Newton et al., 2011), consistent with the Sr isotope and fossil evidence (section 5.3). Combined, these data suggest that the shift toward higher sulfur isotope ratio is coeval to the one observed in Europe across the T-OAE n-CIE. An alternative option would be to restrict the T-OAE n-CIE to the interval of $\delta^{13}C_{org}$ values <30‰ recorded between 0 and 2 m of the composite record at Vilyui. It would then be tempting to correlate the broader n-CIE recorded between 0 and 16 m (Fig. 6) with the expanded $\delta^{13}C_{org}$ n-CIE characterizing the lower Toarcian–lowermost upper Toarcian (transition Bifrons and Variabilis zones) interval in the Kelimyar section (Suan et al., 2011) and in many NW European successions (Küspert, 1982; Burnaz et al., 2024; van de Schootbrugge et al., 2020; Ruebsam et al., 2024). It is worth mentioning that this long-ranging n-CIE has only been reported in TOC-rich (TOC >1 wt%) strata and is absent in the $\delta^{13}C_{skeletal}$ data from Europe (Fig. 6). As suggested for the post T-OAE interval of NW Europe (Suan et al., 2015), this long-ranging n-CIE most probably reflects a higher proportion of ^{13}C-depleted marine organic matter, consistent with the relatively high HI values recorded at Kelimyar, Siberia (Suan et al., 2011), and in N and S Germany (Burnaz et al., 2024; Ruebsam et al., 2024). As explained above (section 5.2.), such a compositional influence at Vilyui (see section 5.1) certainly applies to the basal 2 m of the Suntar Fm., but does not explain the low $\delta^{13}C_{org}$ values recorded in the overlying interval between 2 and 16 m (Fig. 6).

Therefore, the new carbon, sulfur, and strontium isotope data combined with biostratigraphy allow us to correlate the Vilyui River sections with coeval sites from lower latitudes and to confidently identify the Toarcian hyperthermal event (Fig. 6). This correlation indicates that the interval recording the n-CIE is expanded but generally organic-poor in the studied Siberian sites. As such, this study supports previous work indicating that the response to the Toarcian hyperthermal event was regionally variable (e.g., Rodriguez-Tovar and Reolid, 2013; Fantasia et al., 2019; Remirez and Algeo, 2022), with spatiotemporal variability in climate conditions, sediment dynamics, and bottom water oxygenation.

5.5. Implications for sediment dynamics across the T-OAE in shallow Arctic seas

The new data from the Vilyui Basin and the correlation with coeval polar and low latitude sites allow a comprehensive evaluation of the environmental response to the Toarcian hyperthermal. The T-OAE n-CIE at Vilyui River is expanded relative to younger and older levels at the studied site; a feature that is similarly observed in coeval sites, where these two metrics can vary dramatically (Table 1). High relative thicknesses are commonly found in more proximal and discontinuous successions, with most records showing a n-CIE (> 15% of the Toarcian) comparable to that found at Vilyui River. Specific settings such as highly subsiding rift-basins from Morocco, Greenland and England record even more expanded Toarcian strata (>200 m) with a T-OAE n-CIE reaching up to 70 m (Table 1). At Vilyui River, the studied sediments were deposited on the Suntar crystalline High with very low rates of subsidence (Polyansky et al., 2013) and close to a deltaic system (Fig. 1). The accommodation space was therefore most likely very limited, as suggested by the relatively coarse-grained nature, lateral facies variability, and fossil richness of sediments outside the T-OAE. The closest equivalents in terms of depositional dynamics are the Toarcian sections of SW Germany, where the upper Toarcian is also often strongly condensed and discontinuous, with erosive surfaces of regional extent that locally removed entire ammonite subzones or zones (Arp et al., 2021). In NE Germany, marginal T-OAE sections are also represented by fine-grained deposits interrupting coarser-grained strata containing some hiatal erosive surfaces (Zimmermann et al., 2015; Ruebsam et al., 2024).

This expanded record at Vilyui River contrasts with the more distal records from Kelimyar River, located >1000 km north, where the Toarcian is comparably thick (Table 1) but the T-OAE n-CIE is represented by only 1 to 2 m of sediments (Suan et al., 2011). Three factors may have contributed to this relatively expanded record at the more proximal site of Vilyui River. First, it seems very likely that the low-stand near the Pliensbachian–Toarcian transition removed a large volume of sediments and hence created accommodation space, as suggested by the deeply (>20 m) incised valleys immediately pre-dating the T-OAE n-CIE in East Greenland and Morocco (Ahokas et al., 2014; Krencker et al., 2019). We note that coarsening-upward interval below the negative CIE (top of the Tyung Fm) at Vilyui River is rich in glendonites (ikaite pseudomorphs), confirming that the pre-T-OAE marine regression culminated during a phase of marked cooling of polar areas (Suan et al., 2001; Rogov et al., 2023b). Second, accommodation space likely increased dramatically due to the rapid and global (>50 m) rise of the sea-level that took place across the T-OAE n-CIE (Ahokas et al., 2014; Pittet et al., 2014; Krencker et al., 2019), which resulted locally in a > 80 km inland retreat of the coastline along the adjacent Anabar shield (Devyatov et al., 2011; Fig. 1). Third, geochemical data indicate that continental chemical weathering likely increased globally during the Toarcian hyperthermal (Cohen et al., 2004; Brazier et al., 2015; Percival et al., 2016; Kemp et al., 2020). The fine-grained and expanded record from the Vilyui River Basin suggests that climate change, with a shift toward more humid and warmer conditions, may have enhanced chemical weathering and substantially increased clay input in polar regions, consistent with observations from coeval sites in central and northern Europe (e.g., Montero-Serrano et al., 2015; Fantasia et al., 2019). The condensed nature of the n-CIE at Kelimyar River (Fig. 6), however, suggests that the resulting detrital sediments mostly accumulated along continental margins. The expanded record of the T-OAE n-CIE at Vilyui can therefore be seen as a unique signature of dramatic changes in climate, sediment input and sea-level in proximal settings across the T-OAE.

5.6. Seafloor oxygenation and biotic perturbations

The studied sections are overall organic-poor and dominated by Type III kerogen of terrestrial origin (Fig. 3), suggesting deposition under

Table 1
Absolute and relative thickness of the T-OAE n-CIE in Vilyui and other selected sites (Bodin et al., 2016; da Rocha et al., 2016; Fantasia et al., 2019; Hesselbo et al., 2000; Krencker et al., 2019; Küspert, 1982; Suan et al., 2015; Xu et al., 2018). The beginning of the n-CIE is defined when $\delta^{13}C$ values start to decrease; n-CIE terminates when $\delta^{13}C$ values return to pre-n-CIE values..

Site	Country	Tectonic regime	Setting	Subsidence	T-OAE n-CIE (m)	Dominant lithology	Toarcian strata (m)	Dominant lithology	T-OAE n-CIE/ Toarcian strata	Reference
Vilyui (composite)	Russia	Uplifted basement	Marginal	Low	18	Siltstone	49	Silt-sandstone	37%	This study
Kelimyar River	Russia	Passive margin	Basinal	Low	1.5	Claystone	40	Clay	4%	Suan et al. (2011)
Bohrung 1002 Zimmern	Germany	Passive margin	Basinal	Low	3.5	Claystone	14.8	Clay	24%	Küspert (1982)
Yorkshire coast (composite)	England	Extensional passive margin	Basinal	Intermediate	7	Claystone	130	Clay (silt)	5%	Hesselbo et al. (2000); Kemp et al. (2005)
Peniche	Portugal	Extensional rift-basin	Basinal	Intermediate	19	Carb. mud with gravity deposits	200	Carb. mud	10%	Rocha et al. (2014); Fantasia et al. (2019)
Mochras	Wales	Extensional rift-basin	Basinal	High	30	Carb. mud, gravity deposits	260	Carb. mud, silt	12%	Xu et al. (2018)
Albuen-Astartekløft	Greenland	Extensional rift-basin	Marginal	High	60	Sand	125	Sand	48%	Krencker et al. (2019)
Foum Tillicht	Morocco	Extensional rift-basin	Basinal	High	110	Mud with gravity deposits	340	Carb. mud	32%	Bodin et al. (2016)
Amellago	Morocco	Extensional rift-basin	Basinal	High	80	Mud with gravity deposits	540	Carb. mud	15%	Bodin et al. (2016)
Dades Valley (composite)	Morocco	Extensional rift-basin	Marginal	High	70	Ooid sands and bioclastic mudstone	700	Sand	10%	Bodin et al. (2016)

predominantly well-oxygenated conditions and/or poor preservation of marine OM of algal or bacterial origin (Type II kerogen), and/or low marine productivity. An oxygenated sediment-water interface is further supported by the common occurrence of *Tancredia*, an infaunal suspension feeder requiring well-oxygenated seawater (Rogov et al., 2023b).

TOC contents and HI values increase in the earliest Toarcian (basal Suntar Fm) at the onset of the T-OAE n-CIE, indicating increased contribution of labile, hydrogen-rich aquatic OM (Type II kerogen). This may reflect enhanced marine productivity and/or improved preservation, or alternatively a reduced continental contribution. Enhanced preservation would reflect a rapid decrease in bottom-water oxygenation at the onset of the Toarcian hyperthermal. A similar pattern has been documented at different Kelimyar River sites and at numerous lower paleo-latitude sites from central and northern Europe (e.g., Kemp et al., 2022). However, in contrast to most other sites, the TOC-rich interval with elevated HI values is restricted to the lowermost part of the n-CIE (Fig. 3), which may suggest a more rapid recovery of oxygenation in nearshore polar environments compared to more distal settings. Nonetheless, the observed OM trends may have been influenced by the relatively proximal depositional setting of the studied sections and by the influence of the transgressive phase associated with the Toarcian hyperthermal. This is supported by the highest TOC and HI values occurring immediately above the transgressive surface of the basal Suntar Fm. The OM geochemical signature may therefore reflect both enhanced preservation and a greater proportion of marine OM, potentially linked to reduced dilution by terrigenous input during rapid shoreline retrogradation within the transgressive system tract. Conversely, the decrease in TOC and HI values recorded above 39 m may reflect a progradational phase (highstand system tract) associated with increased input of terrigenous OM and siliciclastic sediments.

T_{max} data from Vilyui sections show several excursions to lower values (Fig. 3), providing additional constraints on redox conditions. Given their limited stratigraphic extent, these excursions are unlikely to reflect changes in kerogen maturity and instead probably record shifts toward more labile, hydrogen-rich or sulfur-rich OM (Yang and Horsfield, 2020). The decrease in T_{max} values within the basal 4 m of the Suntar Fm. coincides with higher HI values (Fig. 3), consistent with the presence of hydrogen-rich OM. In contrast, subsequent T_{max} excursions are not associated with higher HI values and may instead reflect increased incorporation of organic sulfur (Type IIS kerogen; Yang and Horsfield, 2020). The formation of sulfur-rich OM is typically favored under anoxic conditions in carbonate-rich settings, where limited Fe availability prevents H_2S removal via pyrite precipitation (e.g., Tribovillard et al., 2006).

Interestingly, the onset of the n-CIE (Fig. 3; first 10 m of the Suntar Fm: 36–46.5 m), which records the lowest T_{max} values yielded no mollusc shells. This absence may indicate adverse conditions at or below the sediment-water interface, potentially anoxic /euxinic, that prevented colonization by both infaunal and epifaunal bivalves during the Toarcian hyperthermal. Notably, the "benthic gap" occurs within the lower half of the n-CIE, which according to our correlations, is synchronous with the "belemnite gap" and the "brachiopod gap", as well as with a proliferation of opportunistic benthic foraminifera observed in both organic-rich and organic-poor sites across NW European and polar regions (Hesselbo et al., 2007; Nikitenko et al., 2013; Xu et al., 2018; Rita et al., 2020; Ullmann et al., 2020; Atkinson et al., 2023).

However, if severe anoxia/euxinia was the primary control on benthic colonization, the reappearance of benthic fauna would be expected immediately above the interval with the lowest T_{max} and highest TOC values (i.e., just above 39 m), rather than only after 46.5 m. This offset suggests that oxygen depletion alone cannot account for the observed faunal pattern. This observation is further supported by the imperfect overlap between intervals of inferred anoxia and benthic absence documented in coeval successions. Indeed, many records exhibit a mismatch between "fossil gaps" and intervals of lowest oxygenation (Hesselbo et al., 2007; Xu et al., 2018; Ullmann et al., 2014, 2020, 2021), pointing to the influence of additional factors, such as temperature, salinity, pH, and nutrient availability. In proximal settings such as the Vilyui sites, enhanced influx of terrigenous material and rapidly changing substrate conditions associated to the Toarcian transgression likely exerted an additional control on benthic ecosystems. In this context, the faunal gap cannot be attributed solely to anoxia/euxinia, but instead reflects the combined effects of multiple stressors, including sedimentary dynamics and associated environmental variabilities. In addition, the lower half of the n-CIE coincides with peak temperatures reconstructed for lower paleo-latitudes (Ruebsam et al., 2020; Ullmann et al., 2020), highlighting thermal stress as a key factor warranting further investigation.

More broadly, the apparent synchronicity of these "fossil gaps" suggests a widespread but still poorly understood disturbance affecting marine ecosystems during the early stage of the Toarcian hyperthermal. This disturbance appears to have impacted organisms occupying different ecological niches (e.g., belemnites, brachiopods, foraminifera, and both infaunal and epifaunal bivalves) across a wide latitudinal gradient, from subtropical to polar environments. Comparison with coeval sites (Fig. 6) further suggests that the recolonization of the seafloor by the shallow infaunal deposit-feeding bivalve *Dacryomya* was broadly synchronous across both polar and lower latitudes settings, potentially representing a characteristic benchmark of the Toarcian hyperthermal ecological recovery.

Finally, the low thermal maturity and expanded record of the Toarcian hyperthermal in the Vilyui area offer an exceptional opportunity to reconstruct the evolution of polar temperatures during this critical period, offering important insights into the response of molluscan communities to the Toarcian hyperthermal and its aftermath.

6. Conclusions

The new litho-, bio- and chemo-stratigraphic data from the Pliensbachian–Toarcian siliciclastic successions of the Vilyui River Basin implies that the n-CIE characterizing the Toarcian hyperthermal is expanded (>15 m) relative to younger and older levels at the study sites. Such an expanded record of the n-CIE points to a dramatic increase in accommodation space in the proximal polar setting during the Toarcian hyperthermal, which we attribute to rapid sea-level rise and increased sediment supply due to accelerated continental weathering and runoff. The Toarcian n-CIE is recorded in finer-grained sediments lying immediately above a disconformity surface truncating sand-, gravel- and glendonite-rich deposits. These observations further support models placing the Toarcian hyperthermal as an event of rapid, climatic-induced transgression following a late Pliensbachian–earliest Toarcian global cooling phase. Increased TOC and HI values in the lowermost Toarcian (base of the Suntar Fm) indicate that this warming coincided with a rapid but transient decrease in seafloor oxygenation. Benthic macrofossils are absent in a more expanded interval of 10 m, suggesting that inhospitable conditions prevented the recolonization of the seafloor during a substantial part of the hyperthermal event, a pattern also seen in lower paleo-latitude marine strata. The new records thus point to a supraregional, near synchronous perturbation of benthic habitats in subtropical and polar seas during the Toarcian hyperthermal that cannot be explained solely in terms of oxygenation. The low thermal maturity and expanded nature of the Toarcian n-CIE record presented herein set the stage for future quantifications of climate changes in polar seas across the Toarcian hyperthermal, and for assessing their role in the corresponding biotic perturbations.

CRediT authorship contribution statement

Alicia Fantasia: Investigation, Funding acquisition, Formal analysis, Writing – original draft. **Thomas Letulle:** Investigation, Formal analysis, Writing – original draft. **Mikhail A. Rogov:** Investigation, Funding acquisition, Writing – review & editing. **Alexey P. Ippolitov:** Investigation, Writing – review & editing. **Oleg A. Lutikov:** Investigation, Writing – review & editing. **Nikolay Zverkov:** Investigation, Writing – review & editing. **Arnauld Vinçon-Laugier:** Validation, Investigation, Writing – review & editing. **Thierry Adatte:** Investigation, Writing – review & editing. **Jorge E. Spangenberg:** Validation, Investigation, Writing – review & editing. **Guillaume Paris:** Investigation, Writing – review & editing. **Jeremy E. Martin:** Investigation, Writing – review & editing. **Christophe Lécuyer:** Validation, Writing – review & editing. **Barbora Krizova:** Investigation, Writing – review & editing. **Mathieu Daëron:** Validation, Investigation, Writing – review & editing. **Guillaume Suan:** Supervision, Project administration, Investigation, Funding acquisition, Formal analysis, Conceptualization, Writing – original draft.

Declaration of competing interest

The authors declare that they have no known competing financial interests or personal relationships that could have appeared to influence the work reported in this paper.

Acknowledgments

This study was supported by the French Agence Nationale de La Recherche (ANR) grant ANR-18-31CE-0020 ('Oxymore' project) to G.S. (T.L., A.V.L., C.L, M.D. and J.E.M.), the RFBR-CNRS International Emerging Action (IEA) grant 205700 ('IsoJuraSib' project)/ 21-55-15015 to G.S and M.R. A.I. and O.L., and Marie Skłodowska-Curie Actions Individual Fellowship 895247 to A.F. The IRISS platform (Nancy) is part of the RéGEF network (Réseau Géochimique et Expérimental Français). We thank Bruno Reynard and Gilles Montagnac for giving us access to the micro-Raman spectroscopy platform, Benjamin Daihl and Benjamin Mironneau for their help with isotopic and Raman analyses, and Ghislaine Broillet for her help with SEM analyses. We thank Matías Reolid and an anonymous reviewer for their helpful and constructive comments on an earlier version of this manuscript.

Appendix A. Supplementary data

Supplementary data to this article can be found online at https://doi.org/10.1016/j.gloplacha.2026.105588.

Data availability

The authors confirm that all data necessary for supporting the scientific findings of this paper have been provided.

References

Ahokas, J.M., Nystuen, J.P., Martinius, A.W., 2014. Stratigraphic signatures of punctuated rise in relative sea-level in an estuary-dominated heterolithic succession: Incised valley fills of the Toarcian Ostreaelv Formation, Neill Klinter Group (Jameson Land, East Greenland). Mar. Pet. Geol. 50, 103–129. https://doi.org/10.1016/j.marpetgeo.2013.11.001.

Arp, G., Gropengießer, S., Schulbert, C., Jung, D., Reimer, A., 2021. Biostratigraphy and sequence stratigraphy of the Toarcian Ludwigskanal section (Franconian Alb, Southern Germany). Zitteliana 95, 57–94. https://doi.org/10.3897/zitteliana.95.56222.

Behar, F., Beaumont, V., Penteado, H.L.D., 2001. Rock-Eval 6 technology: performances and developments. Oil Gas Sci. Tech. 56, 111–134.

Bodin, S., Krencker, F.-N., Kothe, T., Hoffmann, R., Mattioli, E., Heimhofer, U., Kabiri, L., 2016. Perturbation of the carbon cycle during the late Pliensbachian – early Toarcian: New insight from high-resolution carbon isotope records in Morocco. J. Afr. Earth Sci. 116, 89–104. https://doi.org/10.1016/j.jafrearsci.2015.12.018.

Bomou, B., Suan, G., Schlögl, J., Grosjean, A.-S., Suchéras-Marx, B., Adatte, T., Spangenberg, J.E., Fouché, S., Zacaï, A., Gibert, C., Brazier, J.-M., Perrier, V., Vincent, P., Janneau, K., Martin, J.E., 2021. The palaeoenvironmental context of Toarcian vertebrate-yielding shales of southern France (Hérault). Geol. Soc. Lond. Spec. Publ. 514, 121. https://doi.org/10.1144/SP514-2021-16.

Boulila, S., Hinnov, L.A., 2017. A review of tempo and scale of the early Jurassic Toarcian OAE: implications for carbon cycle and sea level variations. Newsl. Stratigr. 50, 363–389.

Bryant, R. N., Houghton, J. L., Jones, C., Pasquier, V., Halevy, I., Fike, D. A. 2023. Deconvolving microbial and environmental controls on marine sedimentary pyrite sulfur isotope ratios. Science 2023 Nov 24;382(6673):912–915.

Bucur, I.I., Reolid, M., 2024. Incidence of the early Toarcian global change on Dasycladales (Chlorophyta) and the subsequent recovery: comparison with end-Triassic mass extinction. Earth-Sci. Rev. 249.

Burnaz, L., Littke, R., Grohmann, S., Erbacher, J., Strauss, H., Amann, F., 2024. Lower Jurassic (Pliensbachian–Toarcian) marine paleoenvironment in Western Europe: sedimentology, geochemistry and organic petrology of the wells Mainzholzen and Wickensen, Hils Syncline, Lower Saxony Basin. Int. J. Earth Sci. 113, 1999–2022. https://doi.org/10.1007/s00531-023-02381-8.

Caswell, B.A., Dawn, S.J., 2019. Recovery of benthic communities following the Toarcian oceanic anoxic event in the Cleveland Basin, UK. Palaeogeography, Palaeoclimatology, Palaeoecology 521, 114–126. https://doi.org/10.1016/j.palaeo.2019.02.014.

Chen, W., Kemp, D. B., He, T., Huang, C., Jin, S., Xiong, Y., Newton, R. J., 2021. First record of the early Toarcian Oceanic Anoxic Event in the Hebrides Basin (UK) and implications for redox and weathering changes, Glob. Planet. Change, volume 207, 103685, ISSN 0921–8181, doi:https://doi.org/10.1016/j.gloplacha.2021.103685.

Cohen, A.S., Coe, A.L., Harding, S.M., Schwark, L., 2004. Osmium isotope evidence for the regulation of atmospheric CO_2 by continental weathering. Geology 32, 157–160. https://doi.org/10.1130/g20158.1.

Courtillot, V., 1994. Mass extinctions in the last 300 million years: one impact and seven flood basalts? Isr. J. Earth Sci. 43, 255–266.

Dagis, A.A., 1974. Toarcian ammonites (Hildoceratidae) of the North Siberia. Transactions of the Instute of Geology and Geophysics. Sib. Branch Ac. Sci. USSR 99, 1–107 (in Russian).

Dera, G., Pellenard, P., Niege, P., Deconinck, J-F., Pucéat, E., Dommergues, J-L., 2009. Distribution of clay minerals in early Jurassic Peritethyan seas: Palaeoclimatic significance inferred from multiproxy comparisons. Palaeogeography, Palaeoclimatology, Palaeoecology 271, 39–51.

Devyatov, V., Knyazev, V., Nikitenko, B., Melnik, O., Glinskikh, L., 2010. Pliensbachian–Toarcian boundary of northeastern Siberia and stratigraphic position of the Kurung Mbr of the Kelimyar Formation (Kelimyar River, Olenek River basin). Otechestvennaya Geol. 5, 105–112.

Devyatov, V., Nikitenko, B., Shurygin, B., 2011. Jurassic paleogeography of Siberia during major changeovers. Novosti Paleontologii i Stratigrafii 16, 87–101.

Duncan, R.A., Hooper, P.R., Rahacek, J., Marsh, J.S., Duncan, A.R., 1997. The timing and duration of the Karoo igneous event, southern Gondwana. J. Geophys. Res. 102, 18127–18138.

El Meknassi, S., Dera, G., Cardone, T., De Rafélis, M., Brahmi, C., Chavagnac, V., 2018. Sr isotope ratios of modern carbonate shells: good and bad news for chemostratigraphy. Geology 46, 1003–1006. https://doi.org/10.1130/G45380.1.

Espitalié, J., Deroo, G., Marquis, F., 1985. La pyrolyse Rock-Eval et ses applications. Deuxième partie. Revue de l'Institut français du Pétrole 40, 755–784.

Fantasia, A., Adatte, T., Spangenberg, J.E., Font, E., Duarte, L.V., Föllmi, K.B., 2019. Global versus local processes during the Pliensbachian–Toarcian transition at the Peniche GSSP, Portugal: a multi-proxy record. Earth Sci. Rev. 198, 102932. https://doi.org/10.1016/j.earscirev.2019.102932.

Ferreira, J., Mattioli, E., Sucherás-Marx, B., Giraud, F., Duarte, L.V., Pittet, B., Suan, G., Hassler, A., Spangenberg, J.E., 2019. Western Tethys early and Middle Jurassic calcareous nannofossil biostratigraphy. Earth Sci. Rev. 197, 102908. https://doi.org/10.1016/j.earscirev.2019.102908.

Frolov, A.O., Mashchuk, I.M., Ivantsov, S.V., 2024. Paleogeography and climates of Europe, Central Asia and Siberia in the early Jurassic. Geosfernye issledovaniya – Geosphere Research 4, 22–43. https://doi.org/10.17223/25421379/33/2.

Gill, B.C., Lyons, T.W., Jenkyns, H.C., 2011. A global perturbation to the sulfur cycle during the Toarcian Oceanic Anoxic Event. Earth Planet. Sci. Lett. 312, 484–496.

Goryacheva, A.A., 2017. Lower Jurassic palynostratigraphy of Eastern Siberia. Stratigr. Geol. Korrelyatsiya 25 (3), 29–60.

Grossman, E. L., Ku, T.-H., 1986. Oxygen and carbon isotope fractionation in biogenic aragonite: temperature effects, Chemical Geology: Isotope Geoscience section, volume 59, Pages 59-74, ISSN 0168–9622, doi:https://doi.org/10.1016/0168-9622(86)90057-6.

Guiserix, D., Albalat, E., Ueckermann, H., Davechand, O., Iaccheri, L. M., Bybee, G., Badenhorst, S., Balter, V., 2022. Simultaneous analysis of stable and radiogenic strontium isotopes in reference materials, plants and modern tooth enamel, Chem. Geol., volume 606, 121000, ISSN 0009–2541, doi:https://doi.org/10.1016/j.chemgeo.2022.121000.

Han, Z., Hu, X., Newton, R.J., He, T., Mills, B.J.W., Jenkyns, H.C., Ruhl, M., Jamieson, R.A., 2023. Spatially heterogenous seawater $\delta^{34}S$ and global cessation of Ca-sulfate burial during the Toarcian oceanic anoxic event. Earth Planet. Sci. Lett. 622, 118404.

Hautmann, M., 2006. Shell mineralogical trends in epifaunal Mesozoic bivalves and their relationship to seawater chemistry and atmospheric carbon dioxide concentration. Facies 52, 417–433. https://doi.org/10.1007/s10347-005-0029-x.

Hesselbo, S.P., Grocke, D.R., Jenkyns, H.C., Bjerrum, C.J., Farrimond, P., Bell, H.S.M., Green, O.R., 2000. Massive dissociation of gas hydrate during a Jurassic oceanic anoxic event. Nature 406, 392–395. https://doi.org/10.1038/35019044.

Hollaar, T.P., Hesselbo, S.P., Deconinck, J.-F., Damaschke, M., Ullmann, C.V., Jiang, M., Belcher, C.M., 2023. Environmental changes during the onset of the late Pliensbachian Event (early Jurassic) in the Cardigan Bay Basin, Wales. Clim. Past 19, 979–997. https://doi.org/10.5194/cp-19-979-2023.

Jenkyns, H.C., 1988. The early Toarcian (Jurassic) Anoxic Event. Stratigraphic, Sedimentary, and Geochemical evidence. Am. J. Sci. 288, 101–151.

Jenkyns, H.C., Grocke, D.R., Hesselbo, S.P., 2001. Nitrogen isotope evidence for water mass denitrification during the early Toarcian (Jurassic) oceanic anoxic event. Paleoceanography 16, 593–603. https://doi.org/10.1029/2000pa000558.

Jones, C.E., Jenkyns, H.C., Coe, A.L., Hesselbo, S.P., 1994a. Strontium isotopic variations in Jurassic and cretaceous seawater. Geochim. Cosmochim. Acta 58, 3061–3074. https://doi.org/10.1016/0016-7037(94)90179-1.

Jones, C.E., Jenkyns, H.C., Hesselbo, S.P., 1994b. Strontium isotopes in early Jurassic seawater. Geochim. Cosmochim. Acta 58, 1285–1301. https://doi.org/10.1016/0016-7037(94)90382-4.

Kasemann, S.A., Klein, T., Boyle, R.A., Ullmann, C.V., Aberhan, M., Meixner, A., Duarte, L.V., Lenton, T.M., Piazza, V., Wood, R.A., 2025. Ocean acidification at the Toarcian Anoxic Event captured by boron isotopes in the lime mud record. Commun. Earth Environ. 6, 533. https://doi.org/10.1038/s43247-025-02510-yKemp et al., 2022.

Kemp, D.B., Coe, A.L., Cohen, A.S., Schwark, L., 2005. Astronomical pacing of methane release in the early Jurassic period. Nature 437, 396–399. https://doi.org/10.1038/nature04037.

Kirina, T.I., 1961. Stratigraphy of the lower Jurassic deposits of the western part of the Vilyui syneclise. Transactions of VNIGRI 249, 18–71 (in Russian).

Knjazev, V.G., Devyatov, V.P., Shurygin, B.N., 1991. Stratigraphy and Paleogeography of the Early Jurassic of the East of the Siberian Platform. Yakutian Scientific Center of SB Ac. Sci. USSR, Yakutsk, p. 100 (in Russian).

Knyazev, V.G., Devyatov, V.P., Kutygin, R.V., Nikitenko, B.L., Shurygin, B.N., 2003. Zonal Standart of the Toarcian Stage of the North-East Part of Asia. YB of the SD RAS Publishing House, Yakutsk, p. 105 (in Russian).

Korte, C., Hesselbo, S.P., Ullmann, C.V., Dietl, G., Ruhl, M., Schweigert, G., Thibault, N., 2015. Jurassic climate mode governed by ocean gateway. Nat. Commun. 6. https://doi.org/10.1038/ncomms10015.

Koshelkina, Z.V., 1961. New data on the stratigraphy of the lower Jurassic marine deposits along the Vilyuy river. Izvestia of the Academy of Sciences of the USSR. Geologic Series 8, 78–86.

Krencker, F.-N., Lindström, S., Bodin, S., 2019. A major sea-level drop briefly precedes the Toarcian oceanic anoxic event: implication for early Jurassic climate and carbon cycle. Sci. Rep. 9, 12518. https://doi.org/10.1038/s41598-019-48956-x.

Küspert, W., 1982. Environmental changes during Oil Shale Deposition as Deduced from Stable Isotope Ratios. In: Einsele, G., Seilacher, A. (Eds.), Cyclic and Event Stratification. Springer, Berlin Heidelberg, pp. 482–501. https://doi.org/10.1007/978-3-642-75829-4_36.

Lécuyer, C., Hutzler, A., Amiot, R., Daux, V., Grosheny, D., Otero, O., Martineau, F., Fourel, F., Balter, V., Reynard, B., 2012. Carbon and oxygen isotope fractionations between aragonite and calcite of shells from modern molluscs, Chemical Geology, Volumes 332–333. ISSN 92-101, 0009–2541. https://doi.org/10.1016/j.chemgeo.2012.08.034.

Letulle, T., Suan, G., Daëron, M., Rogov, M., Lécuyer, C., Vinçon-Laugier, A., Reynard, B., Montagnac, G., Lutikov, O., Schlögl, J., 2022. Clumped isotope evidence for early Jurassic extreme polar warmth and high climate sensitivity. Clim. Past 18, 435–448 doi: cp-18-435-2022.

Little, C.T.S., Benton, M.J., 1995. Early Jurassic mass extinction: a global long-term event. Geology 23, 495–498.

Lutikov, O.A., 2024. Bivalve-Based Stratigraphy of the Toarcian of Eastern Siberia and Northeastern Russia (Family Oxytomidae Ichikawa, 1958). Part 3. Toarcian–Lower Aalenian Zonal Scale Based on Oxytomids. Bivalve-Based Stratigraphy and Correlation. Stratigraphy and Geological Correlation 32, 929–1032. https://doi.org/10.1134/S0869593824700035.

Lutikov, O.A., Arp, G., 2023. A Boreal Toarcian Biochronological Zonation based on Bivalve Molluscs of the Genus Meleagrinella Whitfield, 1885. Stratigraphy and Geological Correlation 31, 49–70. https://doi.org/10.1134/S0869593823020053.

Mailliot, S., Mattioli, E., Bartolini, A., Baudin, F., Pittet, B., Guex, J., 2009. Late Pliensbachian-early Toarcian (early Jurassic) environmental changes in an epicontinental basin of NW Europe (Causses area, Central France): A micropaleontological and geochemical approach. Palaeogeography, Palaeoclimatology, Palaeoecology 273, 346–364.

Martin, J.E., Suan, G., Suchéras-Marx, B., Rulleau, L., Schlögl, J., Janneau, K., Williams, M., Léna, A., Grosjean, A.S., Sarroca, E., Perrier, V., 2021. Stenopterygiids from the lower Toarcian of Beaujolais and a chemostratigraphic context for ichthyosaur preservation during the Toarcian Oceanic Anoxic Event. Geol. Soc. Lond. Spec. Publ. https://doi.org/10.1144/SP514-2020-232.

Maxwell, E.E., Vincent, P., 2016. Effects of the early Toarcian Oceanic Anoxic Event on ichthyosaur body size and faunal composition in the southwest German Basin. Paleobiology 42 (1), 117–126 http://www.jstor.org/stable/44017966.

McArthur, J., Page, K., Duarte, L., Thirlwall, M., Li, Q., Weis, R., Comas-Rengifo, M., 2020. Sr-isotope stratigraphy (Sr-87/Sr-86) of the lowermost Toarcian of Peniche, Portugal, and its relation to ammonite zonations. Newsl. Stratigr. 53, 297–312.

McArthur, J.M., Donovan, D.T., Thirlwall, M.F., Fouke, B.W., Mattey, D., 2000. Strontium isotope profile of the early Toarcian (Jurassic) oceanic anoxic event, the duration of ammonite biozones, and belemnite palaeotemperatures. Earth Planet. Sci. Lett. 179, 269–285.

McElwain, J.C., Wade-Murphy, J., Hesselbo, S.P., 2005. Changes in carbon dioxide during an oceanic anoxic event linked to intrusion into Gondwana coals. Nature 435, 479–482.

Merkel, A., Munnecke, A., 2023. Glendonite-bearing concretions from the upper Pliensbachian (lower Jurassic) of South Germany: indicators for a massive cooling in the European epicontinental sea. Facies 69, 10. https://doi.org/10.1007/s10347-023-00667-6.

Mesezhnikov, M.S., 1966. Zones of regional stratigraphic scales. Soviet Geol. 7, 3–16 (in Russian).

Montero-Serrano, J.-C., Föllmi, K.B., Adatte, T., Spangenberg, J.E., Tribovillard, N., Fantasia, A., Suan, G., 2015. Continental weathering and redox conditions during the early Toarcian Oceanic Anoxic Event in the northwestern Tethys: insight from the Posidonia Shale section in the Swiss Jura Mountains. Palaeogeogr. Palaeoclimatol. Palaeoecol. 429, 83–99.
Müller, T., Jurikova, H., Gutjahr, M., Tomašových, A., Schlögl, J., Liebetrau, V., Duarte, L., v., Milovský R., Suan G., Mattioli E., Pittet B., Eisenhauer A., 2020. Ocean acidification during the early Toarcian extinction event: evidence from boron isotopes in brachiopods. Geology 48, 1184–1188. https://doi.org/10.1130/G47781.1.
Newton, R.J., Reeves, E.P., Kafousia, N., Wignall, P.B., Bottrell, S.H., Sha, J.G., 2011. Low marine sulfate concentrations and the isolation of the European epicontinental sea during the early Jurassic. Geology 39, 7–10. https://doi.org/10.1130/g31326.1.
Nikitenko, B.L., 2008. The early Jurassic to Aalenian paleobiogeography of the Arctic realm: Implication of microbenthos (Foraminifers and Ostracodes). Stratigr. Geol. Correl. 16, 59–80.
Nikitenko, B.L., Shurygin, B.N., Knyazev, V.G., Meledina, S.V., Dzyuba, O.S., Lebedeva, N.K., Peshchevitskaya, E.B., Glinskikh, L.A., Goryacheva, A.A., Khafaeva, S.N., 2013a. Jurassic and cretaceous stratigraphy of the Anabar area (Arctic Siberia, Laptev Sea coast) and the Boreal zonal standard. Russ. Geol. Geophys. 54, 808–837. https://doi.org/10.1016/j.rgg.2013.07.005.
Nikitenko, B.L., Reolid, M., Glinskikh, L., 2013b. Ecostratigraphy of Benthic Foraminifera for Interpreting Arctic Record of Early Toarcian Biotic Crisis (Northern Siberia, Russia). Palaeogeography¸Palaeoclimatology, Palaeoecology 376.
Nordt, L., Breecker, D., White, J., 2022. Jurassic greenhouse ice-sheet fluctuations sensitive to atmospheric CO2 dynamics. Nat. Geosci. 15, 54–59. https://doi.org/10.1038/s41561-021-00858-2.
Page, K.N., 2003. The lower Jurassic of Europe: its subdivision and correlation. GEUS Bulletin 1, 21–59. https://doi.org/10.34194/geusb.v1.4646.
Palfy, J., Smith, P.L., 2000. Synchrony between Early Jurassic extinction, oceanic anoxic event, and the Karoo–Ferrar flood basalt volcanism. Geology 28 (8), 747–750.
Paris, G., Sessions, A.L., Subhas, A.V., Adkins, J.F., 2013. MC-ICP-MS measurement of $\delta^{34}S$ and $\Delta^{33}S$ in small amounts of dissolved sulfate, Chemical Geology, volume 345. ISSN 50-61, 0009–2541. https://doi.org/10.1016/j.chemgeo.2013.02.022.
Paris, G., Fehrenbacher, J.S., Sessions, A.L., Spero, H.J., Adkins, J.F., 2014. Experimental determination of carbonate associated sulfate $\delta^{34}S$ in planktonic foraminifera shells. Geochem. Geophys. Geosyst. 15, 1452–1461. https://doi.org/10.1002/2014gc005295.
Peters, K.E., 1986. Guidelines for evaluating petroleum source rock using programmed pyrolysis. AAPG Bull. 70 (3), 318–329.
Pittet, B., Suan, G., Lenoir, F., Duarte, L.V., Mattioli, E., 2014. Carbon isotope evidence for sedimentary discontinuities in the lower Toarcian of the Lusitanian Basin (Portugal): sea level change at the onset of the Oceanic Anoxic Event. Sediment. Geol. 303, 1–14.
Present, T.M., Paris, G., Burke, A., Fischer, W.W., Adkins, J.F., 2015. Large Carbonate Associated Sulfate isotopic variability between brachiopods, micrite, and other sedimentary components in late Ordovician strata. Earth Planet. Sci. Lett. 432, 187–198. https://doi.org/10.1016/j.epsl.2015.10.005.
Rau, G., Takahashi, T., Marais, D., 1989. Latitudinal variations in plankton δ13C: implications for CO2 and productivity in past oceans. Nature 341, 516–518. https://doi.org/10.1038/341516a0.
Rennie, V.C.F., Paris, G., Sessions, A.L., Abramovich, S., Turchyn, A.V., Adkins, J.F., 2018. Cenozoic record of δ34S in foraminiferal calcite implies an early Eocene shift to deep-ocean sulfide burial. Nat. Geosci. https://doi.org/10.1038/s41561-018-0200-y.
Reolid, M., Ruebsam, W., Benton, M.J., 2022. Dinosaur extinctions related to the Jenkyns Event (early Toarcian, Jurassic). Span. J. Palaeontol. 37 (2), 123–140. https://doi.org/10.7203/sjp.25683.
Reolid, M., Ruebsam, W., Reolid, J., Benton, M.J., 2024. Impact of early Toarcian climatic changes on marine reptiles: Extinction and recovery. Earth-Science Reviews 259.
Polyansky, O.P, Prokop'ev, A.V., Babichev, A.V., Korobeynikov, S.N., Reverdatto, V.V., 2013. The rift origin of the Vilyui basin (East Siberia), from reconstructions of sedimentation and mechanical mathematical modeling. Russ. Geol. Geophys. 54 (2), 121–137. https://doi.org/10.1016/j.rgg.2013.01.001.
da Rocha, R.B., Mattioli, E., Duarte, L.V., Pittet, B., Elmi, S., Mouterde, R., Cabral, M.C., Comas-Rengifo, M.J., Gomez, J.J., Goy, A., Hesselbo, S.P., Jenkyns, H.C., Littler, K., Mailliot, S., Veiga de Oliveira, L.C., Osete, M.L., Perilli, N., Pinto, S., Ruget, C., Suan, G., 2016. Base of the Toarcian stage of the lower Jurassic defined by the Global Boundary Stratotype Section and Point (GSSP) at the Peniche section (Portugal). Episodes 39, 460–481.
Rodriguez-Tovar, F.J., Reolid, M., 2013. Environmental conditions during the Toarcian Oceanic Anoxic Event (T-OAE) in the westernmost Tethys: influence of the regional context on a global phenomenon. Bull. Geosci. 88 (4), 697–712.
Rogov, M., Ershova, V., Gaina, C., Vereshchagin, O., Vasileva, K., Mikhailova, K., Krylov, A., 2023a. Glendonites throughout the Phanerozoic. Earth-Science Reviews 241, 104430. https://doi.org/10.1016/j.earscirev.2023.104430.
Rogov, M.A., Mironenko, A., Ippolitov, A., Lutikov, O., 2023b. A first record of lower Jurassic (Toarcian) coleoid jaws in Siberia. Diversity 15, 742. https://doi.org/10.3390/d15060742.
Ruebsam, W., Müller, T., Kovács, J., Pálfy, J., Schwark, L., 2018. Environmental response to the early Toarcian carbon cycle and climate perturbations in the northeastern part of the West Tethys shelf, Gondwana Research, volume 59. ISSN 144-158, 1342. https://doi.org/10.1016/j.gr.2018.03.013.
Ruebsam, W., Reolid, M., Sabatino, N., Masetti, D., Schwark, L., 2020a. Molecular paleothermometry of the early Toarcian climate perturbation. Global Planet. Change 195.
Ruebsam, W., Reolid, M., Schwark, L., 2020b. $\delta^{13}C$ of terrestrial vegetation records Toarcian CO_2 and climate gradients. Sci. Rep. 10, 117.
Ruebsam, W., Reolid, M., Mattioli, E., Schwark, L., 2022. Organic Carbon Accumulation at the Northern Gondwana Paleomargin (Tunisia) during the Toarcian Oceanic Anoxic Event: Sedimentological and Geochemical Evidence. Palaeogeography, Palaeoclimatology, Palaeoecology, Volume, p. 586.
Ruebsam, W., Franz, M., Ansorge, J., Obst, K., Schwark, L., 2024. Late Triassic to early Jurassic carbon isotope chemostratigraphy and organo-facies evolution in a distal to proximal transect of the north German Basin. International Journal of Earth Sciences 113, 1977–1998. https://doi.org/10.1007/s00531-024-02418-6.
van de Schootbrugge, B., Houben, A.J.P., Ercan, F.E.Z., Verreussel, R., Kerstholt, S., Janssen, N.M.M., Nikitenko, B., Suan, G., 2020. Enhanced Arctic-Tethys connectivity ended the Toarcian Oceanic Anoxic Event in NW Europe. Geol. Mag. 1–19. https://doi.org/10.1017/S0016756819001262.
Slater, S.M., Twitchett, R.J., Danise, S., Vajda, V., 2019. Substantial vegetation response to early Jurassic global warming with impacts on oceanic anoxia. Nat. Geosci. 12, 462–467.
Spangenberg, J.E., 2024. Three combustion reactions in a single EA/IRMS acquisition as a strategy to save helium and energy. Rapid Commun. Mass Spectrom. 38. https://doi.org/10.1002/rcm.9663.
Suan, G., Mattioli, E., Pittet, B., Mailliot, S., Lécuyer, C., 2008. Evidence for major environmental perturbation prior to and during the Toarcian (early Jurassic) oceanic anoxic event from the Lusitanian Basin. Portugal. Paleoceanography 23.
Suan, G., Mattioli, E., Pittet, B., Lécuyer, C., Suchéras-Marx, B., Duarte, L.V., Philippe, M., Reggiani, L., Martineau, F., 2010. Secular environmental precursors to early Toarcian (Jurassic) extreme climate changes. Earth Planet. Sci. Lett. 290, 448–458.
Suan, G., Nikitenko, B.L., Rogov, M.A., Baudin, F., Spangenberg, J.E., Knyazev, V.G., Glinskikh, L.A., Goryacheva, A.A., Adatte, T., Riding, J.B., Föllmi, K.B., Pittet, B., Mattioli, E., Lécuyer, C., 2011. Polar record of early Jurassic massive carbon injection. Earth Planet. Sci. Lett. 312, 102–113.
Suan, G., van de Schootbrugge, B., Adatte, T., Fiebig, J., Oschmann, W., 2015. Calibrating the magnitude of the Toarcian carbon cycle perturbation. Paleoceanography 30, 495–509. https://doi.org/10.1002/2014pa002758.
Svensen, H., Planke, S., Chevallier, L., Malthe-Sørenssen, A., Corfu, F., Jamtveit, B., 2007. Hydrothermal venting of greenhouse gases triggering early Jurassic global warming. Earth Planet. Sci. Lett. 256, 554–566.
Teichert, B.M.A., Luppold, F.W., 2013. Glendonites from an early Jurassic methane seep — climate or methane indicators? Palaeogeogr. Palaeoclimatol. Palaeoecol. 390, 81–93. https://doi.org/10.1016/j.palaeo.2013.03.001.
Thaler, C., Paris, G., Dellinger, M., Dissard, D., Berland, S., Marie, A., Labat, A., Bartolini, A., 2023. Impact of seawater sulfate concentration on sulfur concentration and isotopic composition in calcite of two cultured benthic foraminifera. Biogeosciences 20, 5177–5198. https://doi.org/10.5194/bg-20-5177-2023.
Them, T.R., Gill, B.C., Caruthers, A.H., Gerhardt, A.M., Gröcke, D.R., Lyons, T.W., Marroquín, S.M., Nielsen, S.G., Trabucho Alexandre, T.P., Owens, J.D., 2018. Thallium isotopes reveal protracted anoxia during the Toarcian (early Jurassic) associated with volcanism, carbon burial, and mass extinction. Proc. Natl. Acad. Sci. U. S. A. 115 (26), 6596–6601. https://doi.org/10.1073/pnas.1803478115.
Trabucho-Alexandre, J.P., Gröcke, D.R., Atar, E., Herringshaw, L., Jarvis, I., 2022. A new subsurface record of the Pliensbachian–Toarcian, Lower Jurassic, of Yorkshire. Proc. Yorks. Geol. Soc. 64. https://doi.org/10.1144/pygs2022-007 pygs2022-007.
Trecalli, A., Spangenberg, J.E., Adatte, T., Föllmi, K.B., Parente, M., 2012. Carbonate platform evidence of ocean acidification at the onset of the early Toarcian oceanic anoxic event. Earth Planet. Sci. Lett. 357–358, 214–225.
Tribovillard, N., Algeo, T.J., Lyons, T., Riboulleau, A., 2006. Trace metals as paleoredox and paleoproductivity proxies: an update. Chem. Geol. 232 (1–2), 12–32.
Ullmann, C.V., Thibault, N., Ruhl, M., Hesselbo, S.P., Korte, C., 2014. Effect of a Jurassic oceanic anoxic event on belemnite ecology and evolution. Proc. Natl. Acad. Sci. 111, 10073–10076. https://doi.org/10.1073/pnas.1320156111.
Ullmann, C.V., Frei, R., Korte, C., Hesselbo, S.P., 2015. Chemical and isotopic architecture of the belemnite rostrum. Geochim. Cosmochim. Acta 159, 231–243. https://doi.org/10.1016/j.gca.2015.03.034.
Vaes, B., van Hinsbergen, D.J.J., van de Lagemaat, S.H.A., van der Wiel, E., Lom, N., Advokaat, E.L., Boschman, L.M., Gallo, L.C., Greve, A., Guilmette, C., Li, S., Lippert, P.C., Montheil, L., Qayyum, A., Langereis, C.G., 2023. A global apparent polar wander path for the last 320 Ma calculated from site-level paleomagnetic data. Earth-Science Reviews 245, 0012–8252. https://doi.org/10.1016/j.earscirev.2023.104547.
Xu, W., Ruhl, M., Jenkyns, H.C., Leng, M.J., Huggett, J.M., Minisini, D., Ullmann, C.V., Riding, J.B., Weijers, J.W.H., Storm, M.S., Percival, L.M.E., Tosca, N.J., Idiz, E.F., Tegelaar, E.W., Hesselbo, S.P., 2018. Evolution of the Toarcian (early Jurassic) carbon-cycle and global climatic controls on local sedimentary processes (Cardigan Bay Basin, UK). Earth Planet. Sci. Lett. 484, 396–411. https://doi.org/10.1016/j.epsl.2017.12.037.

Yang, Y., Han, Z., Hu, X., He, T., Newton, R.J., Harvey, J., 2024. Strontium isotope evidence for regional enhanced continental weathering during the early Toarcian in the Tethys Himalaya. Palaeogeogr. Palaeoclimatol. Palaeoecol. 641, 112136.

Zimmermann, J., Franz, M., Heunisch, C., Luppold, F.W., Mönnig, E., Wolfgramm, M., 2015. Sequence stratigraphic framework of the lower and Middle Jurassic in the north German Basin: Epicontinental sequences controlled by Boreal cycles. Palaeogeography, Palaeoclimatology, Palaeoecology 440, 395–416. https://doi.org/10.1016/j.palaeo.2015.08.045.

Zverkov, N.G., Grigoriev, D.V., Danilov, I.G., 2021. Early Jurassic palaeopolar marine reptiles of Siberia. Geol. Mag. 158, 1305–1322. https://doi.org/10.1017/S0016756820001351.